Molecular flexibility of DNA as a key determinant of RAD51 recruitment

Federico Paoletti [1], Afaf El-Sagheer [2,3], Jun Allard [4],
Tom Brown [2], Omer Dushek [1,†], Fumiko Esashi [1,†]

1. Sir William Dunn School of Pathology, University of Oxford, OX1 3RE, UK.
2. Department of Chemistry, University of Oxford, OX1 3TA, UK.
3. Department of Science and Mathematics, Suez University, Suez 43721, Egypt.
4. Department of Mathematics, University of California, Irvine, CA 92697-4575, US.

[†] Equal contribution and corresponding authors:
Omer Dushek: omer.dushek@path.ox.ac.uk
Fumiko Esashi: fumiko.esashi@path.ox.ac.uk

Keywords: Homologous recombination, RAD51, ssDNA, dsDNA, Mathematical model, SPR

Abstract

The timely activation of homologous recombination is essential for the maintenance of genome stability, in which the RAD51 recombinase plays a central role. Biochemically, human RAD51 polymerises faster on single-stranded DNA (ssDNA) compared to double-stranded DNA (dsDNA), raising a key conceptual question: how does it discriminate between them? In this study, we tackled this problem by systematically assessing RAD51 binding kinetics on ssDNA and dsDNA differing in length and flexibility using surface plasmon resonance. By fitting detailed polymerisation models informed by our experimental datasets, we show that RAD51 is a mechano-sensor that exhibits a larger polymerisation rate constant on flexible ssDNA compared to rigid ssDNA or dsDNA. This model presents a new general framework suggesting that the flexibility of DNA, which may increase locally as a result of DNA damage, plays an important role in rapidly recruiting repair factors that multimerise at sites of DNA damage.

Introduction

DNA double-strand breaks (DSBs) are cytotoxic lesions that can lead to chromosomal breaks, genomic instability and tumourigenesis in mammalian cells (Tubbs and Nussenzweig, 2017). Homologous recombination (HR) can offer an error-free DNA repair mechanism to restore genetic information at DSB sites, and in this way, contribute to genome stability. During HR-mediated repair, single-stranded DNA (ssDNA) overhangs are generated and rapidly coated with the ssDNA-binding replication protein A (RPA) (Chen and Wold, 2014). ssDNA-bound RPA is then exchanged for RAD51, the central ATP-dependent recombinase that catalyses HR-mediated repair. RAD51 polymerises on ssDNA to form a ssDNA-nucleoprotein filament and guide homologous strand invasion and DSB repair (Baumann et al., 1996).

The central mechanism of HR is evolutionarily highly conserved, and the bacterial RAD51 ortholog RecA has clear preference to polymerise on ssDNA over dsDNA (Benson et al., 1994). However, human RAD51 shows weaker binding affinity to ssDNA compared to RecA, and the mechanism by which RAD51 polymerises on ssDNA in preference to dsDNA remains enigmatic. Earlier studies using electrophoretic mobility shift assay (EMSA) have suggested that RAD51 binds both ssDNA and dsDNA with similar affinities (Benson et al., 1994), albeit its preferential ssDNA binding was visible in the presence of ammonium sulphate (Shim et al., 2006). These endpoint assays, however, do not provide information as to whether binding kinetics may contribute to a potential RAD51-dependent ssDNA / dsDNA discrimination mechanism. Indeed, more recent kinetic studies have revealed that RAD51 polymerisation consists of two phases: a rate-limiting nucleation phase and a growth phase (Hilario et al., 2009; Miné et al., 2007; Van der Heijden et al., 2007). A minimal polymer nucleus, with a length of either two-to-three or four-to-five RAD51 protomers (Hilario et al., 2009; Van der Heijden et al., 2007), is proposed to elicit the growth phase of RAD51 polymerisation. Intriguingly, RAD51 was shown to display faster association kinetics on ssDNA (Candelli et al., 2014) and slower dissociation kinetics on dsDNA, indicating that the RAD51-

65 dsDNA complex is stable once formed (Miné et al., 2007). However, the mechanism underlying
66 these kinetic differences is unclear.
67
68 A key difference between ssDNA and dsDNA is their molecular flexibility: ssDNA is known to be
69 more flexible compared to dsDNA. The flexibility of a DNA molecule can be characterised by its
70 persistence length (L_p), a mechanical parameter quantifying polymer rigidity: the higher the
71 persistence length, the more rigid the polymer. In the presence of monovalent or divalent salt,
72 dsDNA displays an L_p of ~ 30 - 55 nm (Baumann et al., 1997; Brunet et al., 2015), while ssDNA is
73 much more flexible, with an L_p of 1.5 - 3 nm (Chi et al., 2013; Kang et al., 2014; Murphy et al.,
74 2004). These observations imply that ssDNA can explore a much larger configurational space
75 compared to dsDNA. It follows that the formation of a structured (less flexible) RAD51 polymer on
76 ssDNA will incur a larger entropic energy penalty compared to the formation of a RAD51 polymer
77 on dsDNA. Despite the clear thermodynamic implications of RAD51 polymerisation on DNA, the
78 impact of DNA flexibility on RAD51 nucleoprotein filament formation has been largely overlooked.
79
80 In this study, we describe how RAD51 polymerises on DNA. Using a combination of surface
81 plasmon resonance (SPR) and small-angle x-ray scattering (SAXS), we have assessed the RAD51
82 binding kinetics on DNA using ssDNA and dsDNA oligonucleotides differing in length and flexibility.
83 Analyses of the SPR data using biochemical mathematical models revealed that RAD51
84 polymerisation required a minimal nucleus of four and two molecules on ssDNA and dsDNA,
85 respectively. Interestingly, our analyses further uncovered that RAD51 is a mechano-sensor that
86 polymerises faster on flexible DNA. We hypothesised that the entropic penalty to polymerisation on
87 flexible DNA is offset by a large enthalpic contribution and show this to be the case by perturbing
88 the RAD51 protomer-protomer interaction. We propose the DUET model (**D**na molec**U**lar
89 fl**E**xibili**T**y), which explains the ability of RAD51 to preferentially and stably polymerise on highly

90 flexible ssDNA compared to stiff ssDNA and dsDNA, enabled by the enthalpic energy of RAD51
91 polymerisation.
92

93 Results

94 **RAD51 preferential binding to ssDNA is dependent on the length of DNA template**

95 To evaluate how human RAD51 discriminates between ssDNA and dsDNA, we used SPR to
96 assess the binding kinetics of untagged recombinant human wild-type (WT) RAD51 to a 50-mer
97 mixed base ssDNA molecule (dN-50) and a 50-mer mixed base paired dsDNA molecule (dN-50p).
98 These analyses performed in the presence of ATP and Ca^{2+}, which blocks RAD51 ATP hydrolysis
99 (Bugreev and Mazin, 2004), showed 1) faster RAD51 association to ssDNA compared to dsDNA,
100 and 2) similar RAD51 lifetimes on both ssDNA and dsDNA (**Fig. S1 *A* and *B***). These observations
101 confirm previous findings that WT RAD51 distinguishes ssDNA from dsDNA through faster
102 polymerisation on ssDNA (Candelli et al., 2014), validating SPR as a sensitive experimental
103 system to determine RAD51 binding kinetics to DNA.
104

105 We then aimed to define the initial steps of RAD51 association with ssDNA. To this end, we
106 generated a series of mixed base short ssDNA oligos with varying lengths, each of which can be
107 bound by a restricted number of RAD51 molecules. As a single RAD51 molecule engages with
108 three nucleotides of DNA (Short et al., 2016), a ssDNA consisting of 5 nucleotides (dN-5), 8
109 nucleotides (dN-8), 11 nucleotides (dN-11), 14 nucleotides (dN-14) and 17 nucleotides (dN-17) can
110 accommodate up to one, two, three, four and five RAD51 molecules, respectively (**Fig. 1*A***). Our
111 systematic SPR measurements of WT RAD51 binding kinetics revealed no RAD51 binding to the
112 dN-5, dN-8 and dN-11, slow association and moderate dissociation with dN-14, and slightly faster
113 association and slow dissociation with dN-17 (**Fig. 1 *A* and *B***). These observations suggested that
114 three or less RAD51 molecules are unable to generate a stable nucleus on ssDNA, four RAD51

115 molecules form a quasi-stable nucleus, and five or more RAD51 molecules are able to form a
116 highly stable nucleus.
117
118 To similarly evaluate the initial steps of RAD51 association with dsDNA, we generated an
119 analogous series of mixed base dsDNA consists of 5 base pairs (dN-5p), 8 base pairs (dN-8p) and
120 11 base pairs (dN-11p), which can accommodate up to one, two or three RAD51 molecules,
121 respectively (**Fig. 1*C***). Our SPR measurement detected no RAD51 binding to the dsDNA dN-5p,
122 as was the case for the ssDNA dN-5. To our surprise, however, we detected slow association and
123 moderate dissociation of WT RAD51 with the dN-8p, and even faster association and slower
124 dissociation with the dN-11p (**Fig. 1*D***). These observations initially suggested that one RAD51
125 molecule is unable to associates stably with dsDNA, but two RAD51 molecules form a quasi-stable
126 nucleus, and three or more RAD51 molecules are able to form a highly stable nucleus. This
127 suggested that WT RAD51 nucleation on dsDNA requires only 2-3 RAD51 molecules versus 4-5
128 on ssDNA. Altogether, these observations supports the idea that WT RAD51 can bind more
129 strongly to short (≤ 11 bp) dsDNA compared to short (≤ 11 nt) ssDNA molecules, but binds more
130 strongly to long (50 nt) ssDNA molecules compared to long (50 bp) dsDNA molecules.
131
132 **RAD51 polymerisation on ssDNA is promoted by faster adsorption and / or elongation**
133 **compared to dsDNA**
134 Informed by these SPR datasets, we developed ODE models describing RAD51 polymerisation on
135 ssDNA and dsDNA, that could be simultaneously fit to all corresponding SPR curves. This
136 approach would enable us to determine the mechanistic differences in RAD51 polymerisation
137 kinetics on ssDNA and dsDNA.
138
139 The polymerisation of RAD51 in solution was based on mass action kinetics with a maximum
140 length of 16 (see Supplementary Information for details). The model allows any RAD51 n-mer (1 ≤

141 n < 16) to associate with any other RAD51 m-mer (1 ≤ m < 16) to form an (m + n)-mer (1 < m + n
142 ≤ 16). In addition, any RAD51 k-mer can fall apart in every possible combination of m-mers and n-
143 mers (k = n + m) (e.g. a pentamer can fall apart to form a monomer and a tetramer, or a dimer and
144 a trimer). This model provides the concentrations of RAD51 polymers in solution, and is solved in
145 the steady-state so that it only depends on a single fit parameter K_D (i.e. the RAD51 promoter-
146 promoter dissociation constant). The predicted concentrations are then inserted into the kinetic
147 models to describe RAD51 polymerisation on ssDNA and dsDNA.
148
149 The next two kinetic models described the sequential formation of RAD51 polymers on ssDNA and
150 on dsDNA. We tested models of increasing complexity based on mass action kinetics until we
151 identified models that were able to fit the experimental datasets (see Supplementary Information
152 for details). Both the ssDNA and dsDNA models allow for the adsorption of any RAD51 n-mer from
153 solution onto DNA (provided at least n DNA binding sites are available), given that n-mers (1 ≤ n ≤
154 16) can exist in solution. Polymer elongation occurs when a RAD51 m-mer in solution binds to a
155 DNA-bound n-mer to form a DNA-bound (n+m)-mer, provided that at least n + m DNA binding sites
156 are available and 1 < m + n ≤ 16. However, unbinding was assumed to only take place via single
157 protomer dissociation and via the dissociation of short RAD51 nuclei. This is a valid assumption
158 when considering that in all the SPR experiments in this study ATP hydrolysis is inhibited via the
159 addition of Ca^{2+}, leading to slow RAD51 filament disassembly which can be approximated as
160 disassembly via monomer removal or via the removal of short, unstable RAD51 nuclei. The ssDNA
161 model consists of a polymerisation forward rate constant (k_p), an unstable reverse rate constant
162 (k_u), a quasi-stable reverse rate constant (k_q), and a stable reverse rate constant (k_s). k_p describes
163 the adsorption and elongation of RAD51 polymers on ssDNA up to a maximum length of 16, k_u
164 describes the dissociation of unstable nuclei (1-3 RAD51 molecules), k_q describes the dissociation
165 of quasi-stable nuclei (4 RAD51 molecules), and k_s describes the dissociation of single RAD51
166 protomers (i.e. RAD51 monomers of a RAD51 polymer) (**Figs. 1*A* and 2*A***). Similarly, kinetic model

167 for dsDNA includes k_p, k_u, and k_s, but without the need for k_q to describe dissociation of quasi-
168 stable nuclei (i.e. 2 RAD51 molecules) (**Fig. 1*C***). For dsDNA, k_u describes the rate of dissociation
169 of RAD51 monomers not bound to a RAD51 polymer (**Fig. 2*B***).
170
171 Using ABC-SMC to fit these models to the ssDNA dN-X data (**Fig. 1*B***) and the dsDNA dN-Xp data
172 (**Fig. 1*D***), values for the model parameters were determined (**Fig. 2 *A* and *B*, S2)**. This analysis
173 identified a nano-molar range RAD51 protomer-protomer dissociation constant (dN-X and dN-Xp
174 K_D = 1.14 ± 0.5 nM) as a key factor driving rapid RAD51 polymerisation on both ssDNA and
175 dsDNA, similarly to other studies using either pressure perturbation fluorescence spectroscopy
176 (Schay et al., 2016) or single molecule fluorescence microscopy (Candelli et al., 2014). This is due
177 to the fact that this K_D value enables WT RAD51 to form abundant long polymers in solution at
178 both 150 nM and 3 μM [WT RAD51] (**Fig. 2 *C* and *D***). These RAD51 polymers can then directly
179 adsorb onto DNA and elongate, therefore enabling WT RAD51 to polymerise faster on the dN-50
180 and dN-50p (150 nM [WT RAD51]) compared to the dN-14, dN-17, dN-11p and dN-8p oligos (3 μM
181 [WT RAD51]) despite a 20-fold lower RAD51 injection concentration.
182
183 Importantly, we also identified a 6.5-fold higher ssDNA polymerisation forward rate constant (dN-X
184 k_p = (2.6 ± 1.8) × 10^{-2} /μM/s) compared to dsDNA (dN-Xp k_p = (4 ± 0.6) × 10^{-3} /μM/s), explaining the
185 overall faster RAD51 polymerisation on ssDNA (**Fig. 2 *A* and *B***). Overall, these analyses suggest
186 that WT RAD51 adsorption and/or elongation is faster on ssDNA compared to dsDNA, and that a
187 high protomer-protomer affinity enables WT RAD51 to nucleate and elongate effectively on ssDNA
188 and dsDNA even at low concentrations of RAD51.
189
190 **RAD51 polymerises faster on flexible DNA**
191 Overall, our analyses suggest that WT RAD51 can nucleate more efficiently on short dsDNA
192 molecules but polymerises significantly faster on long ssDNA molecules. We speculate that the

193 difference in RAD51 polymerisation speed is due to the higher flexibility of ssDNA compared to
194 dsDNA. Explicitly, we propose a Bend-To-Capture (BTC) mechanism to explain how DNA flexibility
195 can impact polymerisation kinetics (**Fig. 3*A***). A free RAD51 monomer or polymer in solution would
196 need to generate two sequential, non-covalent interactions to be incorporated into the growing
197 polymer: the interaction with the exposed interface of an existing RAD51 polymer and with the
198 exposed scaffold DNA. To avoid steric clashes, we reasoned that each of these interactions
199 requires naked DNA immediately next to the existing RAD51 polymer in a configuration that can
200 bend away from the preferred direction of the polymer. In this way, flexible DNA is expected to
201 explore more conformations compatible with the further addition of RAD51 per unit time.
202
203 To test this notion, we designed an experiment to measure the kinetics of WT RAD51 binding to
204 DNA oligos of varying flexibility. It has been shown that poly-dT ssDNA, which is widely used for
205 RAD51 binding assays, is highly flexible, while poly-dA ssDNA is highly rigid due to base stacking
206 interactions (Mills et al., 1999) (Sim et al., 2012)**.** Consistently, our SAXS-derived persistence
207 length measurements showed ssDNA dT-50 is the most flexible oligo, followed by dN-50, dA-50
208 and dsDNA dN-50p (**Fig. S3 and Table 1**). By measuring RAD51 binding kinetics to these DNA
209 oligos (**Fig. 3*B*)**, we found that WT RAD51 indeed displayed faster association to the dT-50
210 compared to the dN-50, and the model fit suggests this is due to a higher polymerisation rate
211 constant (k_p) (**Fig. 3 *C* and *D***). Furthermore, WT RAD51 displayed very slow association to the dA-
212 50, comparable to that of dsDNA dN-50p, which is explained by a lower polymerisation rate
213 constant (**Fig. 3 *C* and *D***). Conversely, individually fitting the unstable reverse rate constant (k_u),
214 the quasi-stable reverse rate constant (k_q) or the stable reverse rate constant (k_s) cannot explain
215 the ssDNA dT-50 or dA-50 data (**Fig. S4 *A*-*C***). In addition, for RAD51 DNA-bound polymers of
216 length greater than 3, the fractions of RAD51 in each polymer state are similar on ssDNA dT-50,
217 dN-50, dA-50 and dsDNA dN-50p, suggesting WT RAD51 forms a similar proportion of polymers
218 length 4 - 16 across the four DNA molecules (**Fig. S4*D***). Finally, we observed that the lifetime of

219 DNA-bound RAD51 protomers was independent of the flexibility of the underlying DNA (**Fig. 3*E***).
220 Taken together, these observations suggest that although WT RAD51 is able to form a stable
221 nucleus with fewer molecules on dsDNA compared to ssDNA (two versus five), it elongates and/or
222 adsorbs more efficiently on ssDNA because of its higher flexibility, consistent with our proposed
223 BTC mechanism.
224
225 **RAD51 protomer-protomer interaction compensates for the entropic penalty of flexible DNA**
226 So far, we have observed that WT RAD51 associates faster to flexible ssDNA compared to
227 dsDNA, and the proposed BTC mechanism describes how higher DNA flexibility can induce faster
228 RAD51 polymerisation. However, the formation of a stiff RAD51 polymer on highly flexible DNA is
229 expected to be associated with a large entropic penalty because RAD51 polymerisation stiffens
230 ssDNA and dsDNA to a similar extent ($L_p \sim 200$ nm for both RAD51-ssDNA and RAD51-dsDNA
231 complexes)(Miné et al., 2007), therefore dramatically reducing the number of spatial configurations
232 that a flexible DNA polymer can explore. RAD51 polymerisation on flexible ssDNA is expected to
233 incur a higher entropic penalty compared to its polymerisation on stiff ssDNA or dsDNA (**Fig. 3*B***,
234 "Entropic penalty"). Since we do not observe this in the WT data, we hypothesized that the
235 enthalpic contribution of WT RAD51 polymerisation on DNA is sufficiently large to dominate any
236 entropic penalty to associate with ssDNA and dsDNA (**Fig. 3*B***, "WT RAD51 enthalpic
237 contribution"). However, if this enthalpic contribution was to be reduced, our model predicts that at
238 equilibrium there would be less RAD51 bound to flexible DNA compared to stiff DNA. We define
239 this as the Entropic Penalty Compensation (EPC) mechanism, which proposes that the favourable
240 enthalpic energy of RAD51 polymerisation on DNA is sufficient to compensate for any DNA-
241 dependent entropic penalty. Specifically, we predict that, upon reduction of the enthalpic
242 contribution, RAD51 will exhibit faster unbinding from flexible DNA compared to stiff DNA, as this is
243 consistent with both reduced RAD51 binding at equilibrium and faster binding due to the Bent-to-
244 Capture mechanism (**Fig. 4*A***).

245

246 To directly test this hypothesis, we assessed the kinetics of a RAD51 mutant, which confers a
247 reduced enthalpic contribution compared to WT RAD51. We predicted that, with such a mutation,
248 the stability of the mutant RAD51 polymers on DNA would become more dependent on the
249 flexibility of the underlying DNA (**Fig. 4 *A* and *B***). We took advantage of a phenylalanine to
250 glutamate substitution at RAD51 residue 86 (F86E), which reduces the RAD51 protomer-protomer
251 interaction affinity (Pellegrini et al., 2002; Esashi et al., 2007; Yu et al., 2003). Indeed, using size-
252 exclusion chromatography with multi-angle light scattering (SEC-MALS), we confirmed that F86E
253 RAD51 is primarily monomeric in solution (**Fig. S5 *A-C***). We then used SPR to measure the
254 binding kinetics of F86E RAD51 to ssDNA dT-50, dN-50, dA-50 and dsDNA dN-50p, and used
255 ABC-SMC to fit a simplified polymerisation model simultaneously to all four data sets (**Fig. 4*D***).
256 Importantly, we fit a single reverse rate ($k_{pr} = k_u = k_q = k_s$) to the F86E RAD51 SPR data, given that
257 the F86E RAD51 binding kinetics to the short ssDNA oligos (dN-5, dN-8, dN-11, dN-14, dN-17)
258 and dsDNA oligos (dN-5p, dN-8p, dN-11p) were not systematically measured due to low F86E
259 purification yield. It was immediately evident that F86E RAD51 shows significantly reduced affinity
260 for ssDNA and dsDNA compared to WT RAD51, with no detectable binding to DNA at the
261 concentration of 150 nM or 3 μM (**Fig. S5 *D* and *E***). Nonetheless, at 30 μM, we observed F86E
262 RAD51 displays faster elongation on more flexible DNA (**Fig. 4 *B* and *E*, Fig. S6**), as we observed
263 for WT RAD51 (**Fig. 3 *C* and *D***). Additionally, DNA-binding at 30 μM can be explained by the fact
264 that F86E RAD51 (K_D = 10.2 ± 7 μM) only forms abundant, nucleus-size polymers in solution (2-5
265 RAD51 molecules) at 30 μM [F86E RAD51] (**Fig. 4 *F* and *G***). This is in contrast to WT RAD51 (K_D
266 = 1.14 ± 0.5 nM), which can form abundant, long polymers in solution at 150 nM or 3 μM [WT
267 RAD51] (**Fig. 2 *C* and *D***). Strikingly, F86E RAD51 displayed reduced lifetimes ($1/k_{pr}$) that inversely
268 correlated with the flexibility of DNA (**Fig. 4*H***). This observation is in sharp contrast with WT
269 RAD51, which formed stable, long-lived polymers independently of DNA flexibility (**Fig. 3*E***). Taken
270 together, these observations support the notion that the enthalpic contribution of WT RAD51

271 polymer formation is sufficient to offset the large entropic penalty associated with polymerisation
272 on flexible DNA. As a result, RAD51 is able to polymerise more rapidly on flexible DNA despite
273 incurring a larger entropic penalty.
274

275 Discussion

276 In this study, we have analysed the kinetics of RAD51 binding to ssDNA and dsDNA oligos of
277 varying length and flexibility *via* a combination of SPR, SAXS and mathematical modelling to
278 understand how RAD51 discriminates between ssDNA and dsDNA. Based on our observations,
279 we propose the DUET (**D**na molec**U**lar fl**E**xibili**T**y) model, which describes how RAD51
280 polymerises on ssDNA in preference to dsDNA: 1) RAD51 has a faster polymerisation rate
281 constant on flexible DNA because flexible DNA explores more conformations compatible with
282 RAD51 binding per unit time (the BTC mechanism) (**Fig. 3*A***), and 2) the enthalpic contribution of
283 RAD51 polymerisation enables RAD51 to overcome the entropic penalty to binding to flexible DNA
284 (the EPC mechanism) (**Fig. 4*A***).
285

286 The diploid human genome consists of 6.4 billion base pairs and ~ 50 endogenous DSBs are
287 estimated to occur in every cell cycle (Vilenchik and Knudson, 2003)**.** In human cells, the resection
288 step of HR-mediated DSB repair can generate ssDNA overhangs up to 3.5 k nucleotides in length
289 (Zhou et al., 2014)**,** which then serve as a platform for RAD51 polymerisation. Given that ssDNA
290 overhangs would constitute only ~ 0.005 % of the total genomic DNA (3.5 k nucleotides x two
291 overhangs x 50 DSBs / 6.4 billion base pairs), the polymerisation of RAD51 on resected ssDNA
292 needs to be greatly directed. The average nuclear concentration of RAD51 is estimated at ~ 100
293 nM (Reuter et al., 2014), and several RAD51 mediators, such as BRCA2, PALB2 and RAD52,
294 contribute to increase the RAD51 local concentration at DSBs and/or RAD51 binding to ssDNA,
295 while preventing its association with dsDNA (Buisson et al., 2010; Carreira and Kowalczykowski,
296 2011; Jensen et al., 2010; Ma et al., 2017a; Miyazaki et al., 2004; Zhao et al., 2015). Nonetheless,

297 to date, *in vivo* evidence that these RAD51 mediators are sufficient to promote RAD51
298 polymerisation on DSB-derived ssDNA in preference to the bulk of undamaged dsDNA is limited.
299
300 It is important to note that resected ssDNA is first bound by RPA prior to RAD51 polymerisation.
301 RPA is a heterotrimer complex with six-OB folds, four of which can associate tightly with ssDNA in
302 a stepwise manner (Fan and Pavletich, 2012; Zou et al., 2006). RPA binding to ssDNA is believed
303 to eliminate ssDNA secondary structures to facilitate RAD51 polymerisation. Significantly, previous
304 kinetic studies have demonstrated a rapid exchange of ssDNA-bound RPA with free RPA available
305 in solution, a phenomenon defined as 'facilitated exchange' (Ma et al., 2017b). Given that one RPA
306 heterotrimer has a footprint of 30 nucleotides and one RAD51 protomer binds to 3 nucleotides of
307 ssDNA (Short et al., 2016), the dissociation of a single RPA heterotrimer would expose enough
308 ssDNA to accommodate up to ten RAD51 molecules. Hence, it is reasonable to speculate that
309 RPA dissociation provides highly flexible ssDNA, which in turn can promote the adsorption and
310 elongation steps of RAD51 polymerisation.
311
312 Another major unanswered question regarding RAD51 polymerisation is how RAD51 can
313 distinguish ssDNA generated by DSB resection from ssDNA formed during normal cellular
314 processes, such as DNA replication and transcription. Spontaneous RAD51 polymerisation on all
315 ssDNA would be problematic, as it may trigger undesired, toxic recombination events or disruption
316 of DNA replication and transcription, causing genomic instability. In this context, the DUET model
317 is particularly appealing: ssDNA generated during transcription and replication does not have free
318 ends and could therefore be less flexible compared to resected ssDNA with a free 3' overhang.
319 This in turn may limit RAD51 polymerisation on transcription- and replication-derived ssDNA, while
320 promoting it on flexible ssDNA at DSBs. Intriguingly, a recent report demonstrated that poly(dA)
321 stretches at replication forks are more vulnerable to DNA damage as they are unprotected by RPA,
322 conforming early-replicating fragile sites (Tubbs et al., 2018). Our study further suggests that such

323 poly(dA)-associated DNA damage is less efficiently repaired by RAD51-mediated HR, increasing
324 genome instability at these loci.
325
326 It should be pointed out, however, that this study has built on the RAD51 kinetics detectable in the
327 presence of Ca^{2}+ which blocks RAD51-mediated ATP hydrolysis. This condition slows down
328 RAD51 dissociation from DNA, hence enabling sensitive detection of RAD51 binding to short DNA
329 substrates, which is otherwise challenging. Nonetheless, future studies to support our findings
330 under conditions allowing RAD51's ATP hydrolysis will shed further light on the dynamics of
331 RAD51 polymerisation on DNA. Most significantly, this work paves the way for further work to
332 include the impact of other HR mediator proteins, such as BRCA2 and RAD51 paralogs (Shahid et
333 al., 2014; Taylor et al., 2016), to elaborate genome integrity control mechanisms.
334
335 Beyond HR repair, this study suggests a general framework to understand how DNA binding
336 proteins are recruited to sites of DNA damage. Numerous DNA repair machineries are composed
337 of multiple subunits with several binding interfaces to DNA and other co-factors. It is therefore
338 tempting to speculate that broken DNA ends may enhance recruitment of such repair complexes
339 simply due to increased DNA flexibility. In line with this notion, increased mobility of broken DNA
340 has been demonstrated in mammalian cells (Aten et al., 2004; Cho et al., 2014; Aymard et al.,
341 2017). Hence, this work presents a conceptual advancement in linking DNA repair and DNA
342 flexibility, adding an important dimension which should be taken account of when assessing repair
343 process both in biochemical assays and in cellular contexts.
344

345 Material and methods

346 RAD51 Mutagenesis

347 The bacterial expression vector pET11d (Merck-Millipore) carrying the human WT RAD51 (WT-
348 pET11d) was used as a template for the PCR-mediated QuikChange site-directed mutagenesis

349 (Agilent Technologies) to introduce F86E substitution (F86E-pET11d) with a forward primer 5'-
350 GCTAAATTAGTTCCAATGGGTGAGACC ACTGCAACTGAATTCCACC - 3' and a reverse primer
351 5'- GGTGGAATTCAGTTGCAGTGGTCT CACCCATTGGAACTAATTTAGC - 3'.
352
353 **RAD51 Protein Purification**
354 To express RAD51, Rosetta 2 (DE3) pLysS cells (Novagen) carrying the WT-pET11d or F86E-
355 pET11d were grown in LB media containing 100 µg/ml ampicillin and 25 µg/ml chloroamphenicol,
356 and by adding 0.5 mM IPTG at OD_{595} = 0.6, protein expression was induced. Cell pellets were
357 resuspended in PBS and mixed with the equal volume of lysis buffer (3 M NaCl, 100 mM Tris-HCl
358 pH 7.5, 4 mM EDTA pH 8, 20 mM ß-mercaptoethanol, Sigma Protease Inhibitor Cocktail (Sigma)).
359 The suspension was sonicated and spun at 20k rpm with a 45 Ti rotor (Beckman). The supernatant
360 was slowly mixed with 0.1 % polyethylenimine at 4°C for 1 hour and spun at 20K rpm using a 45 Ti
361 rotor to remove DNA. The supernatant was then slowly mixed with an equal volume of 4 M
362 ammonium sulphate (2 M final concentration) at 4°C for 1 hour and spun at 10 K rpm using a JA-
363 17 rotor (Beckman). Pellets containing RAD51 were suspended in 25 ml of resuspension buffer
364 (0.5 M KCl, 50 mM Tris-HCl pH 7.5, 1 mM EDTA, 2 mM DTT, 10 % glycerol) and spun again at
365 20k rpm to remove residual DNA. The supernatant was then dialysed overnight at 4°C in TEG
366 buffer (50 mM Tris pH 7.5, 1 mM EDTA, 2 mM DTT, 10 % glycerol) containing 200 mM KCl
367 (TEG200). For F86E RAD51, the cell lysate was prepared as for WT RAD51, and dialysed
368 overnight at 4°C in TEG buffer containing 50 mM KCl (TEG75).
369
370 RAD51 purification was carried out by chromatography at 4°C using the AKTA Pure Protein
371 Purification System (GE Healthcare). For WT RAD51, the dialysed WT RAD51 containing sample
372 was loaded onto a 5 ml HiTrap Heparin column (GE Healthcare) and eluted *via* a linear gradient of
373 200 mM – 600 mM KCl. The peak fractions were pooled and dialysed in TEG200, and
374 concentrated on a 1 ml HiTrap Q column (GE Healthcare) followed by the isocratic elusion with
375 TEG buffer containing 600 mM KCl (TEG600). Peak fractions containing WT RAD51 were dialysed

376 in SPR buffer (150 mM KCl, 20 mM Hepes pH 7.5, 2 mM DTT, 10 % glycerol), aliquoted, snap
377 frozen and stored at -80°C. Similarly, the dialysed F86E RAD51 containing cell lysate was
378 fractionated through a 5 ml HiTrap Heparin column, but with a linear gradient of 75 mM – 600 mM
379 KCl. The flow-through and F86E RAD51 peak fractions were pooled and dialysed in TEG buffer
380 containing 50 mM KCl (TEG50) and reloaded onto a 5 ml HiTrap Heparin column. Following a 50
381 mM – 600 mM KCl linear gradient elution, F86E RAD51 peak fractions were pooled and dialysed in
382 TEG buffer containing 100 mM KCl (TEG100). The sample was concentrated on a 1 ml HiTrap Q
383 column followed by TEG600 isocratic elution. Peak fractions were applied on a 24 ml Superdex200
384 10/300 GL size-exclusion column (GE Healthcare), and fractions containing monometic F86E
385 RAD51 were pooled and dialysed in TEG100. F86E RAD51 was then re-concentrated using a 1 ml
386 HiTrap Q column and TEG600 isocratic elution. The peak fractions were dialysed in SPR buffer,
387 aliquoted, snap frozen and stored at -80°C.
388
389 **Multi-Angle Light Scattering**
390 To confirm the monomeric status of F86E RAD51, the peak size-exclusion chromatography F86E
391 RAD51 elution fraction was serially diluted (5, 1:1 serial dilutions) and loaded onto a Superdex200
392 10/300 GL size exclusion column (GE Healthcare) equilibrated with MALS Buffer (150 mM KCl, 50
393 mM Tris pH 7.5, 1 mM EDTA, 2 mM DTT). Each elution was analysed using a Wyatt Heleos8+ 8-
394 angle light scatterer linked to a Shimadzu HPLC system comprising LC-20AD pump, SIL-20A
395 Autosampler and SPD20A UV/Vis detector. Data collection was carried out at the Department of
396 Biochemistry, University of Oxford. Data analysis was carried out using the ASTRA software
397 (Wyatt).
398
399 **DNA Oligo and Duplex Synthesis**
400 The dN-5p, dN-8p and dN-11p dsDNA sequences were designed as two complimentary ssDNA
401 sequences connected *via* two units of hexaethylene glycol (flexible linker). The dN-5, dN-8, dN-11
402 ssDNA molecules were designed using one of the two corresponding dsDNA annealing

403 sequences. The dN-14 and dN-17 ssDNA molecules were designed by extending one of the two
404 dN-11p dsDNA annealing sequences. Standard DNA phosphoramidites, solid supports, 3'-Biotin-
405 TEG CPG and additional reagents were purchased from Link Technologies Ltd and Applied
406 Biosystems Ltd. All oligonucleotides were synthesized on an Applied Biosystems 394 automated
407 DNA / RNA synthesizer using a standard 1.0 *μ*mole phosphoramidite cycle of acid-catalyzed
408 detritylation, coupling, capping, and iodine oxidation. Stepwise coupling efficiencies and overall
409 yields were determined by the automated trityl cation conductivity monitoring facility and in all
410 cases were >98.0%. All β-cyanoethyl phosphoramidite monomers were dissolved in anhydrous
411 acetonitrile to a concentration of 0.1 M immediately prior to use. The coupling time for normal A, G,
412 C, and T monomers was 60 s, and the coupling time for the hexaethylene glycol phosphoramidite
413 monomer (from link) was extended to 600 s. Cleavage of the oligonucleotides from the solid
414 support and deprotection was achieved by exposure to concentrated aqueous ammonia solution
415 for 60 min at room temperature followed by heating in a sealed tube for 5 h at 55 °C. Purification of
416 oligonucleotides was carried out by reversed-phase HPLC on a Gilson system using a Brownlee
417 Aquapore column (C8, 8 mm x 250 mm, 300 Å pore) with a gradient of acetonitrile in
418 triethylammonium bicarbonate (TEAB) increasing from 0% to 50% buffer B over 20 min with a flow
419 rate of 4 ml/min (buffer A: 0.1 M triethylammonium bicarbonate, pH 7.0, buffer B: 0.1 M
420 triethylammonium bicarbonate, pH 7.0 with 50% acetonitrile). Elution of oligonucleotides was
421 monitored by ultraviolet absorption at 295 or 300 nm. After HPLC purification, oligonucleotides
422 were freeze dried then dissolved in water without the need for desalting. All oligonucleotides were
423 characterised by negative-mode HPLC-mass spectrometry using either a Bruker micrOTOFTM II
424 focus ESI-TOF mass spectrometer with an Acquity UPLC system, equipped with a BEH C18
425 column (Waters) or a Waters Xevo G2-XS QT mass spectrometer with an Acquity UPLC system,
426 equipped with an Acquity UPLC oligonucleotide BEH C18 column (particle size: 1.7 μm; pore size:
427 130 Å; column dimensions: 2.1 x 50 mm). Data were analysed using Waters MassLynx software or
428 Waters UNIFI Scientific Information System software.
429

430 **Small Angle X-Ray Scattering**

431 The flexibilities of the ssDNA dT-50, ssDNA dN-50, ssDNA dA-50 and the dsDNA dN-50p
432 molecules were assessed using small-angle x-ray scattering (SAXS) at the Diamond Light Source
433 (Harwell, UK). SAXS data were collected using a size exclusion KW 402.5 (2.4 ml) column
434 (Shodex). 50 µl of DNA sample was injected and elution was carried out at 37°C at 75 µl/min using
435 SPR running buffer in the absence of glycerol and BSA. The flexible cylinder model was fit to the
436 four scattering data sets within the 0.0037 - 0.27 [1/Å] range to derive the persistence lengths.
437 Data plotting and fitting was carried out using the SasView software for SAXS data analysis.

438

439 **Surface Plasmon Resonance**

440 The binding kinetics of WT and F86E RAD51 on ssDNA and dsDNA were assessed *via* surface
441 plasmon resonance (SPR) using a Biacore T200 (GE Healthcare). CM5 SPR chip flow cells were
442 activated by injecting 100 µl of a 1:1 N-Hydroxysuccinimide (NHS), ethyl(dimethylaminopropyl)
443 carbodiimide (EDC) mix at 10 µl/min. 100 µl of purified streptavidin (1 mg/ml) was then injected
444 over the flow cells at 10 µl/min. Unbound amine groups were then deactivated by injecting 50 µl of
445 1 M ethanolamine-HCl. 50 µl of 10 mM glycine pH 2.5 was injected to remove uncoupled, sterically
446 bound streptavidin. For all experiments, ~ 8 - 15 RU of biotinylated DNA substrates were
447 immobilised onto either flow cells 2, 3 or 4. After DNA immobilisation, 10 µl of purified biotin was
448 injected over all four flow cells at 10 µl/min to block the remaining free streptavidin binding sites.
449 Chip activation and ligand immobilisation steps were carried out at 25°C. Using high performance
450 injections, the CM5 chip surfaces were then primed *via* 10 injections of 10 µl SPR running buffer
451 (150 mM KCl, 20 mM Hepes pH 7.5, 2 mM DTT, 5 mg/ml BSA, 2.5 mM ATP pH 7.5, 10 mM $CaCl_2$,
452 10 % glycerol) at 30 µl/min. WT or F86E RAD51 diluted in SPR running buffer to the specified
453 concentration was injected at 30 µl/min (association), followed by the injection of SPR running
454 buffer for 20 minutes at 30 µl/min (dissociation) at 37°C.

455

456 **SPR Data Processing**

457 SPR traces were processed using the BIAEvaluation software (GE Healthcare) as following. First,
458 the negative control flow cell trace (Fc1 or Fc3) was subtracted from the experimental flow cell
459 trace. The trace was then vertically and horizontally aligned, such that the start of the protein
460 injection occurs at time = 0 s, Response = 0 RU. Subsequently, the drift trace between the
461 negative control flow cell and the experimental flow cell during the final priming injection was
462 subtracted from the experimental flow cell trace (double-referencing) (Myszka, 1999). All
463 experimental curves were normalised using the following equation:

464

465 $$N = S / (L * (M_{RAD51} / M_{DNA}))$$

466

467 N is the normalised signal (mean number of RAD51 molecules per DNA oligo), S is the signal in
468 RU units (1 RU ~ 50 pg/mm^2), L is the amount of DNA ligand immobilised onto the experimental
469 flow cell (RU), M_{RAD51} is the molecular weight (kDa) of RAD51 (~ 37 kDa) and M_{DNA} is the
470 molecular weight (kDa) of the immobilised DNA molecule. The normalised signal represents the
471 mean number of RAD51 molecules bound to an immobilised DNA molecule, and has a predicted
472 maximum at 16 (i.e. the predicted maximum number of RAD51 molecules bound to a ssDNA or
473 dsDNA 50mer).

474

475 **Mathematical Model Development and Analysis**

476 The ODE model describing RAD51 polymerisation on DNA consists of an equilibrium sub-model
477 and a kinetic sub-model. The equilibrium sub-model was formulated using second order mass-
478 action kinetics *via* the rule-based modelling language BioNetGen (Harris et al., 2016) and consists
479 of 16 non-linear ODEs describing the formation of RAD51 polymers in solution up to a maximum
480 length of 16 (i.e. the predicted maximum number of RAD51 molecules binding to a DNA 50-mer

481 (Short et al., 2016)). Each ODE describes the rate of change in concentration of a RAD51 polymer
482 in solution with respect to time. They are non-linear because monomeric RAD51 is consumed in
483 the process of polymerisation to form RAD51 polymers. In this sub-model, we assume any RAD51
484 n-mer ($1 \leq n < 16$) can bind to any other RAD51 m-mer ($1 \leq m < 16$) to form a RAD51 (n+m)-mer
485 ($1 < n + m \leq 16$). In addition, any RAD51 k-mer can fall apart in every possible combination of m-
486 mers and n-mers ($k = n + m$) (e.g. a pentamer can fall apart to form a monomer and a tetramer, or
487 a dimer and a trimer). The single dissociation constant (K_D) describing all of these pairwise
488 interactions is a fit parameter derived from the SPR data. The model is evaluated at equilibrium to
489 calculate the concentration of each RAD51 polymer in solution, prior to the SPR injection. The
490 concentration distribution of RAD51 polymers in solution depends on the fit parameter K_D. The
491 predicted concentrations of RAD51 polymers are then inserted into the kinetic sub-model.
492
493 The kinetic sub-models describe the formation of RAD51 polymers on DNA. Importantly, during
494 SPR injections the concentrations of RAD51 polymers in solution in the flow cell remains constant
495 because RAD51 is continuously replenished by flow. For this reason, the kinetic sub-models were
496 formulated using first order mass-action kinetics *via* the rule-based modelling language BioNetGen
497 (Harris et al., 2016) and each consist of 17 linear ODEs describing the change in concentration of
498 RAD51-polymer-bound DNA molecules. The extra ODE describes unbound DNA molecules. See
499 Supplementary Information for full details of model development.
500
501 For WT RAD51, ABC-SMC was carried in MATLAB 2016b to determine a unique set of
502 parameters for the equilibrium and kinetic sub-models that can simultaneously explain the ssDNA
503 dN-X data (Figs. 1*B*, 2*A*, S2) and the dsDNA dN-Xp data (Figs. 1*D*, 2*B*, S2). dN-X & dN-Xp K_D, dN-
504 X k_p, k_q, k_s, and dN-Xp k_p are well determined. dN-X k_u and dN-Xp k_u were undetermined, due to
505 the fact that 1) no RAD51 binding was observed to the dN-8 and dN-5p oligos, and 2) the
506 concentration of RAD51 monomers, dimers and trimers in solution at 3 μM [WT RAD51] is low

507 relative to longer polymers (Fig. 2*C*). Finally, we could only determine a well-defined upper bound
508 for the dsDNA stable reverse rate constant (dN-Xp $k_s < 10^{-3}$). For F86E RAD51, ABC-SMC was
509 carried out in MATLAB 2016b to determine a unique set of parameters for the equilibrium sub-
510 model and a simplified version of the kinetic sub-model (Fig. 4*D*) that can simultaneously explain
511 the ssDNA dT-50, dN-50, dA-50 and the dsDNA dN-50p data (Figs. 4*C*, *E*, *H*, S6). All parameters
512 except dN-50p k_{pr} were well determined. dN-50p k_{pr} has a well defined upper bound (i.e. dN-50p k_{pr}
513 $< 10^{-3}$).
514
515 All data and scripts are freely available via:
516 https://osf.io/28cqv/
517
518 **Statistical Analysis**
519 Unpaired, Mann-Whitney-Wilcoxon tests were carried out to test for significant differences between
520 the different fitted RAD51 polymerisation rates and lifetimes (Fig. 3 *D* and *E*, Fig. 4 *E* and *H*). All
521 tests were carried out using GraphPad Prism 7.

522 **Table 2. The list of DNA oligos used in this study.**

Oligo Name	Mass (kDa)	Sequence
ssDNA dN-5	2.057	5'-CGGAC-Biotin TEG-3'
dsDNA dN-5p	4.286	5'-CGGAC **LL** GTCCG-Biotin TEG-3'
ssDNA dN-8	2.594	5'-CTGACTGC- Biotin TEG-3'
dsDNA dN-8p	6.139	5'-CTGACTGC **LL** GCAGTCAG-Biotin TEG-3'
ssDNA dN-11	3.926	5'-CGTCGATAGGC-Biotin TEG-3'
dsDNA dN-11p	7.993	5'-CGTCGATAGGC **LL** GCCTATCGACG-Biotin TEG-3'
ssDNA dN-14	4.872	5'-CGTCGATGAGCAGT-Biotin TEG-3'
ssDNA dN-17	5.795	5'-CGTCGATGAGCAGTGTC-Biotin TEG-3'
ssDNA dN-50	15.682	5'-Biotin-TTGAGAGAGCAGACCACAATTATCACCTACACGACATCATTTTATATCAA-3'
dsDNA dN-50p	31.157	(Forward) 5'-Biotin-TCGAGAGGGTAAACCACAATTATCGCCTACCCAAAACTATTTTATATCAA-3' (Reverse) 5'-TTGATATAAAATAGTTTTGGGTAGGCGATAATTGTGGTTTACCCTCTCGA-3'
ssDNA dT-50	15.541	5'-Biotin-TTTTTTTTTTTTTTTTTTTTTTTTTTTTTTTTTTTTTTTTTTTTTTTTTT-3'
ssDNA dA-50	15.992	5'-Biotin-AAAAAAAAAAAAAAAAAAAAAAAAAAAAAAAAAAAAAAAAAAAAAAAAAA-3'

523

524 **L**: hexaethylene glycol flexible linker. **Biotin TEG**: Biotin linked to a flexible triethylene glycol
525 spacer. **Biotin**: Biotin linked to a standard C6 spacer. **dN**: mixed base composition. **dT**:
526 deoxythymine. **dA**: deoxyadenine.

527 ## Author contributions

528 FE, OD and FP conceived and planned the project. FP conducted all SPR experiments, protein
529 purification and mathematical modelling. AES and TB designed and generated the short DNA
530 oligos for SPR experiments. JA contributed to the conceptualisation of the thermodynamic impact
531 of polymerisation. FE, OD and FP wrote the manuscript with input from all contributing authors.
532

533 ## Acknowledgements

534 FE and OD are supported by Wellcome Trust Senior Research Fellowships in Basic Biomedical
535 Science (101009/Z/13/Z and 207537/Z/17/Z, respectively). JA is supported by National Science
536 Foundation grant (DMS 1454739). TB is thankful for the support by Biotechnology and Biological
537 Sciences Research Council (BB/J001694/2). FP is a recipient of the Systems Biology Doctoral
538 Training Centre Scholarship, funded by the Engineering and Physical Sciences Research Council.
539 We thank Marcus Bridge for assistance with SPR, Nicola Trendel for assistance with ABC-SMC,
540 David Staunton for the SEC-MALS analysis of the RAD51 mutant, and Robert Rambo for the DNA
541 oligo SAXS analysis. We also acknowledge the use of the University of Oxford Advanced
542 Research Computing (ARC) facility in carrying out this work (
543 http://dx.doi.org/10.5281/zenodo.22558).
544

545 ## Competing interests

546 We declare no financial and non-financial competing interests on this study.

547 ## Figure & Table Legends

548 **Table 1**. Persistence lengths (L_p) ± 95% confidence intervals are estimated from fitted Kuhn
549 lengths for the ssDNA dN-50, dA-50, dT-50 and the dsDNA dN-50p SAXS plots. All data
550 manipulation and model fitting were done using SasView. It is likely that the relatively low dsDNA
551 dN-50p L_p of 7.34 nm compared to the average dsDNAp L_p of 30 - 55 nm (Baumann et al., 1997;
552 Brunet et al., 2015) is due to the low GC content of the dN-50p (36%).

553

554 **Figure 1. Kinetics of WT RAD51 binding to ssDNA and dsDNA oligos of varying length.**
555 ***A***. Biotinylated ssDNA oligos of indicated lengths were separately immobilised onto SPR CM5
556 chips *via* biotin-streptavidin interaction. Wild-type (WT) RAD51 was injected at the indicated
557 concentrations to measure association and dissociation kinetics. ***B***. The dotted and solid curves
558 respectively show the binding of RAD51 to the ssDNA oligos measured by SPR and the ODE
559 model fits (see Fig. 2*A* for model description). ***C***. As in *A*, except biotinylated dsDNA molecules of
560 indicated lengths were used to measure association and dissociation kinetics. ***D***. The dotted and
561 solid curves respectively show the binding of RAD51 to the dsDNA oligos measured by SPR and
562 the ODE model fits (see Fig. 2*B* for model description).

563

564 **Figure 2. Mathematical models describing WT RAD51 polymerisation kinetics on ssDNA**
565 **and dsDNA**.
566 ***A.*** Kinetic representation of the ordinary differential equation (ODE) model describing WT RAD51
567 polymerisation on ssDNA, consisting of five parameters: k_p (polymerisation forward rate), k_u
568 (unstable reverse rate), k_q (quasi-stable reverse rate), k_s (stable reverse rate) and K_D (protomer-
569 protomer interaction affinity). K_D predicts the concentrations of RAD51 polymers of variable length
570 in solution, while k_p, k_u, k_q and k_s predict the speed of formation of RAD51 polymers on ssDNA. ***B***.
571 Kinetic representation of the ODE model describing WT RAD51 polymerisation on dsDNA,
572 consisting of four parameters: k_p, k_u, k_s, K_D. K_D predicts the concentrations of RAD51 polymers of

573 variable length in solution, and k_p, k_u and k_s predict the speed of formation of RAD51 polymers on
574 dsDNA. In panels *A* and *B*, purple arrows depict a simplified cartoon representation of RAD51
575 polymerisation in solution. The model allows for any RAD51 n-mer ($1 \leq n < 16$) to associate with
576 any other RAD51 m-mer ($1 \leq m < 16$) to form an (m+n)-mer ($1 < m + n \leq 16$), and any RAD51 k-
577 mer to dissociate into any combination of n-mers and m-mers ($k = n + m$). The ssDNA and dsDNA
578 models were calibrated by simultaneously fitting the SPR curves of ssDNA dN-X (dN-8, dN-14, dN-
579 17, dN-50) and dsDNA dN-Xp (dN-5p, dN-8p, dN-11p, dN-50p) using the mode ABC-SMC
580 particles. Mean values ± 1 SD of 3 mode ABC-SMC particles derived from model fits of 3 dN-X
581 and dN-Xp repeats (n = 3). ssDNA k_p, k_u, k_q and k_s were fit to the ssDNA SPR curves, and dsDNA
582 k_p, k_u and k_s were fit to the dsDNA SPR curves. A single K_D was fit to all curves. ***C***. Predicted
583 concentrations of WT RAD51 polymers in solution at equilibrium as a function of WT RAD51
584 monomer concentration (150 nM, 3 μM, 30 μM), prior to RAD51 injection onto DNA-coated SPR
585 CM5 chips. ***D***. Predicted % WT RAD51 within each polymer state in solution at equilibrium as a
586 function of WT RAD51 monomer concentration (150 nM, 3 μM, 30 μM), prior to RAD51 injection
587 onto DNA-coated SPR CM5 chips. In panels *C* and *D*, the K_D was fixed to the mean value identified
588 in Figs. 2 *A* and *B* (i.e. K_D = 1.14 nM), and the concentration of WT RAD51 monomer concentration
589 was varied accordingly. In panel *D*, the % WT RAD51 values were calculated by multiplying the
590 polymer concentrations by their respective polymer length, and dividing each value by the total
591 RAD51 monomer concentration (i.e. % WT RAD51 = [*n*-mer] * *n* / [WT $RAD51_{monomer}$]). [WT
592 $RAD51_{monomer}$] was calculated via coomassie staining image quantification using a BSA standard
593 curve. It is important to note that the assumed maximum polymer length in solution (16-mer) leads
594 to an overestimation of the concentration of each n-mer in solution, given that RAD51 is likely to
595 form polymers of length greater than 16 at 150 nM, 3 μM and 30 μM WT RAD51 monomer
596 concentration. However, this overestimation is likely to not alter the conclusion that WT RAD51
597 forms long polymers in solution at 150 nM - 30 μM concentration.
598

599 **Figure 3**. **Kinetics of WT RAD51 binding to DNA of varying flexibility.**

600 ***A***. A depiction of the Bend-to-Capture (BTC) mechanism. RAD51 generates two sequential, non-
601 covalent interactions (a RAD51 protomer-protomer interaction and a RAD51-DNA interaction, or
602 *vice versa*) faster on flexible DNA (depicted as ssDNA) compared to rigid DNA (depicted as
603 dsDNA). The free RAD51 monomer or polymer in solution (here depicted as a monomer) to be
604 incorporated into the growing polymer is shown with an asterisk. ***B***. Biotinylated DNA molecules of
605 varying flexibility were separately immobilised onto SPR CM5 chips *via* biotin-streptavidin
606 interaction, and WT RAD51 was injected at the indicated concentrations to measure association
607 and dissociation kinetics. The flexibility of respective DNA, the expected entropic penalties upon
608 RAD51 binding to corresponding DNA and enthalpic contribution of WT RAD51 are indicated in
609 gray, green and blue boxes. H and L in each box denote high and low, respectively. ***C***. WT
610 RAD51 SPR curves for respective DNA oligos (dotted lines) and ODE model fits (solid lines). ***D***
611 **and *E***. Bar plots of fitted k_p values (*D*) and k_s values (*E*) for each SPR curves. In panel *D*, all
612 parameters except k_p were fixed to the mean values as identified in Fig. 2 *A* and *B*, and k_p was
613 fitted using lsqcurvefit (MATLAB). In panel *E*, all parameters except k_s and k_p were fixed to the
614 mean values as identified in Fig. 2 *A* and *B*, and k_s and k_p were fitted using lsqcurvefit (MATLAB).
615 Only the k_s values are reported here. Mean ± 1 SD of 3 ODE model fits (n=3). *D*: un-paired, one-
616 tailed Mann-Whitney-Wilcoxon tests. *E*: un-paired, two-tailed Mann-Whitney-Wilcoxon tests. * $p \leq$
617 0.05; ns = non-significant.

618

619 **Figure 4. Kinetics of monomeric F86E RAD51 binding to DNA of varying flexibility.**

620 ***A***. A depiction of the Entropic Penalty Compensation (EPC) mechanism. The enthalpic contribution
621 of WT RAD51 polymerisation enables RAD51 to overcome the entropic penalty to binding flexible
622 DNA (here depicted as ssDNA). F86E RAD51 has a lower RAD51 protomer-protomer affinity and a
623 consequent lower enthalpic contribution to polymerisation, and thus cannot overcome the entropic
624 penalty for binding to flexible DNA. Both WT and F86E RAD51 can overcome the modest entropic

625 penalty to binding stiff DNA (here depicted as dsDNA). Thick arrows indicate fast capture and fast
626 unbinding, while thin arrows indicate slow capture and slow unbinding. ***B***. As in Fig. 3*B*, but F86E
627 RAD51 was injected at the indicated concentration to measure association and dissociation
628 kinetics. The flexibility of respective DNA, the expected relative entropic penalties upon F86E
629 RAD51 binding to each DNA molecule and enthalpic contribution of F86 RAD51 are indicated in
630 gray, green and blue boxes. H and L shown in each box indicate high and low, respectively. ***C.***
631 F86E RAD51 SPR curves (dotted lines) and corresponding model fits (solid lines) using the model
632 shown in panel *D*. Using ABC-SMC, individual forward rates (k_p) and reverse rates (k_{pr}) were fitted
633 to each experimental curve, while a single K_D was fitted to all experimental curves. ***D***. Kinetic
634 representation of the ordinary differential equation (ODE) model describing F86E RAD51
635 polymerisation on ssDNA and dsDNA, consisting of three parameters: k_p (polymerisation forward
636 rate), k_{pr} (polymerisation reverse rate), K_D (protomer-protomer dissociation constant). The K_D
637 predicts the concentrations of F86E RAD51 polymers of variable length in solution, while k_p and k_{pr}
638 predict the speed of formation of F86E RAD51 polymers on ssDNA and dsDNA. A simplified model
639 compared to the models in Fig. 2 *A* and *B* was used for F86E RAD51 because the kinetics of F86E
640 RAD51 to the dN-5, dN-5p, dN-8, dN-8p, dN-11, dN-11p, dN-14 and dN-17 were not systematically
641 assessed due to low F86E purification yield. The predicted K_D value for F86E is shown. Mean
642 value of mode particles ± 1 SD derived from the ABC-SMC fits (n=3). ***E***. Bar plots of fitted k_p values
643 for the SPR curves. Mean values of mode particles ± 1 SD derived from the ABC-SMC fits (n=3).
644 Un-paired, one-tailed Mann-Whitney-Wilcoxon tests. * $p \leq 0.05$; ns = non-significant. ***F***. Predicted
645 concentrations of F86E RAD51 polymers in solution at equilibrium as a function of F86E RAD51
646 monomer concentration (150 nM, 3 μM, 30 μM), prior to RAD51 injection onto DNA-coated SPR
647 CM5 chips. ***G***. Predicted % F86E RAD51 within each polymer state in solution at equilibrium as a
648 function of F86E RAD51 monomer concentration (150 nM, 3 μM, 30 μM), prior to RAD51 injection
649 onto DNA-coated SPR CM5 chips. In panels *F* and *G*, the K_D was fixed to the mean value identified
650 in Fig. 4*D* (i.e. K_D = 10.2 μM), and the concentration of F86E RAD51 monomer concentration was

651 varied accordingly. In panel *G*, the % F86E RAD51 values were calculated by multiplying the
652 polymer concentrations by their respective polymer length, and dividing each value by the total
653 RAD51 monomer concentration (i.e. % F86E RAD51 = [*n*-mer] * *n* / [F86E $RAD51_{monomer}$]). [F86E
654 $RAD51_{monomer}$] was calculated via coomassie staining image quantification using a BSA standard
655 curve. ***H.*** Bar plots of fitted k_{pr} values for the SPR curves. Mean values of mode particles ± 1 SD
656 derived from the ABC-SMC fits (n=3). Un-paired, one-tailed Mann-Whitney-Wilcoxon tests. * $p \leq$
657 0.05; ns = non-significant.
658
659 **Figure S1. The experimental setup.**
660 ***A***. Depiction of the experimental setting. A biotinylated DNA oligo is immobilised onto a surface
661 plasmon resonance (SPR) CM5 chip *via* biotin-streptavidin interaction. RAD51 protein is injected
662 over the DNA-coated SPR matrix to measure polymerisation kinetics. Throughout this period,
663 association and dissociation of RAD51 take place simultaneously. Following protein injection
664 (stop), running buffer is injected to measure dissociation kinetics. ***B***. Wild-type (WT) RAD51 SPR
665 curves for ssDNA dN-50 and dsDNA dN-50p. RAD51 was injected at 150 nM in the presence of
666 2.5 mM ATP (pH 7.5) and 10 mM $CaCl_2$. Curves were normalised to the R_{max}, whereby the
667 normalised response value of X (vertical axis) indicates the average number of RAD51 molecule
668 bound to a single DNA oligo.
669
670 **Figure S2. ABC-SMC for WT RAD51 SPR data fitting**.
671 ABC-SMC probability densities for the simultaneous WT RAD51 ssDNA (Fig. 2*A*) and dsDNA
672 model (Fig. 2*B*) fits of the ssDNA dN-X (Fig. 1*B*) and dsDNA dN-Xp (Fig. 1*D*) SPR data. Heat
673 maps indicate particle frequencies and describe any pair-wise correlations between model
674 parameters (dN-X & dN-Xp K_D, dN-X k_p, k_u, k_q, k_s, dN-Xp k_p, k_u, k_s). All heat map axes are in log-log
675 scale and are labelled according to the corresponding parameter colour: dN-X & dN-Xp K_D (purple),
676 dN-X k_p (orange), dN-X k_u (brown), dN-X k_q (black), dN-X k_s (green), dN-Xp k_p (yellow), dN-Xp k_u

677 (cyan), dN-Xp k_s (blue). A high particle frequency corresponds to a good model fit to the data for
678 the specified parameter pair. The probability densities for individual parameters are presented
679 along the top left diagonal and were estimated using a Gaussian kernel. Particles were initialised
680 *via* log-uniform priors with the following lower and upper bounds: 10^{-4} < dN-X & dN-Xp K_D < 10^{-1},
681 10^{-4} < dN-X k_p < 10^4, 10^{-6} < dN-X k_u < 10^3, 10^{-6} < dN-X k_q < 10^3, 10^{-6} < dN-X k_s < 10^3, 10^{-4} < dN-Xp
682 k_p < 10^4, 10^{-6} < dN-Xp k_u < 10^3, 10^{-6} < dN-Xp k_s < 10^3. PD: probability density.
683
684 **Figure S3. The flexibility measurements of DNA oligos used in this study.**
685 ***A-D.*** The flexibilities of ssDNA dT-50 (A), dN-50 (B), dA-50 (C) and dsDNA dN-50p (D) were
686 assessed by small-angle x-ray scattering (SAXS). The left panels show the absolute scattering
687 intensity (cm^{-1}) measured as a function of the scattering vector ($Å^{-1}$). The flexible cylinder model
688 was fit to the data (fitting range: 0.0037 - 0.27 $Å^{-1}$) to predict the kuhn lengths (persistence length =
689 kuhn length / 2). The right panels show residuals of the flexible cylinder model fits.
690
691 **Figure S4**. **Evaluation of WT RAD51 ssDNA model for ssDNA of variable flexibility.**
692 ***A-C.*** RAD51 SPR curves (dotted lines) for the ssDNA dT-50, dN-50 and dA-50 were fitted by
693 varying a single parameter of the ssDNA model using lsqcurvefit (MATLAB). Each panel shows the
694 ODE model based on varying the unstable reverse rate constant (k_u) (***A***), the quasi-stable reverse
695 rate constant (k_q) (***B***), and the stable reverse rate constant (k_s) (***C***). Individually varying either k_u,
696 k_q, or k_s does not generate accurate model fits. dN-X $\mathbf{k_u}$ was undetermined (Fig. 2*A*), and for this
697 reason fit values in A are reported only as means. ***D***. Model prediction of the % WT RAD51 in
698 different length polymers on ssDNA dN-50, dT-50, dA-50, and dsDNA dN-50p after a 60 second
699 injection of WT RAD51 using models from Fig. 2 *A* and *B*. Parameter values in the ssDNA model
700 were set to the mean values as identified in Fig. 2*A*, and % WT RAD51 values were calculated by
701 multiplying the polymer concentrations by their respective polymer length and dividing each value
702 by the total amount of RAD51 bound to DNA after a 60 second injection (i.e. % WT RAD51 = [*n*-

703 mer] * *n* / [WT RAD51$_{total\ DNA\text{-}bound}$]). dN-X and dN-Xp $\mathbf{k_u}$ were undetermined (Fig. 2 *A* and *B*), and
704 for this reason the values for % WT RAD51 in monomers, dimers, and trimers were not reported
705 and labelled as NA (not-applicable).
706
707 **Figure S5**. **Biochemical characterisation of F86E RAD51 used in this study.**
708 ***A.*** Purified WT and F86E RAD51 on an SDS-PAGE gel are visualized by coomassie blue staining.
709 ***B.*** Size-exclusion multi-angle light scattering (SEC-MALS) curves for F86E RAD51 at five injection
710 concentrations as indicated. The Superdex200 10/300 GL size exclusion column leads to a ~ 10-
711 fold dilution of the injected sample. Hence, approximate elution concentrations are given in
712 brackets below the injection concentrations. Dotted lines represent the molar mass derived values
713 for each elution peak, solid lines represent light scattering. F86E RAD51 concentrations are shown
714 in both mg/ml and μM. ***C.*** Calculated molecular weights of the five F86E RAD51 elution peaks.
715 Data were analysed using the ASTRA 6.1 chromatography software for SEC-MALS. RSE: relative
716 standard error. ***D* and *E.*** F86E RAD51 displays reduced affinity for ssDNA and dsDNA. F86E
717 RAD51 SPR binding curves for the ssDNA dT-50 (D) and the dsDNA dN-50p (E) at the colour-
718 coded concentrations are shown.
719
720 **Figure S6. ABC-SMC for F86E RAD51 kinetic data fitting**.
721 ABC-SMC probability densities for the F86E RAD51 ssDNA/dsDNA model (Fig. 4*D*) fit of the
722 ssDNA dN-50, dA-50, dT-50 and dsDNA dN-50p SPR data. All four SPR curves were fit
723 simultaneously using the same model. k_p and k_{pr} values were individually fit to each curve. A single
724 K_D was fit to all four curves. Heat maps indicate particle frequencies and describe any pair-wise
725 correlations between model parameters (dT-50 & dN-50 & dA-50 & dN-50p K_D, dT-50 k_p, k_{pr}, dN-50
726 k_p, k_{pr}, dA-50 k_p, k_{pr}, dN-50p k_p, k_{pr}). All heat map axes are in log-log scale and are labelled
727 according to the corresponding parameter colour: dN-X & dN-Xp K_D (purple), dT-50 k_p (blue), dT-50
728 k_{pr} (cyan), dN-50 k_p (green), dN-50 k_{pr} (light green), dA-50 k_p (red), dA-50 k_{pr} (salmon), dN-50p k_p

729 (black), dN-50p k_{pr} (grey). A high particle frequency corresponds to a good model fit to the data for
730 the specified parameter pair. The probability densities for individual parameters are presented
731 along the top left diagonal and were estimated using a Gaussian kernel. Particles were initialised
732 *via* log-uniform priors with the following lower and upper bounds: $10^{-4} < K_D < 10^3$, $10^{-6} <$ dT-50 $k_p <$
733 10^4, $10^{-6} <$ dT-50 $k_{pr} < 10^3$, $10^{-6} <$ dN-50 $k_p < 10^4$, $10^{-6} <$ dN-50 $k_{pr} < 10^3$, $10^{-6} <$ dA-50 $k_p < 10^4$, $10^{-6} <$
734 dA-50 $k_{pr} < 10^3$, $10^{-6} <$ dN-50p $k_p < 10^4$, $10^{-6} <$ dN-50p $k_{pr} < 10^3$. PD: probability density.

735 **References**

736 Aten JA, Stap J, Krawczyk PM, van Oven CH, Hoebe RA, Essers J, Kanaar R. (2004). Dynamics
737 of DNA double-strand breaks revealed by clustering of damaged chromosome domains.
738 Science *303*, 92-5.

739 Aymard, F., Aguirrebengoa, M., Guillou, E., Javierre, B.M., Bugler, B., Arnould, C., Rocher, V.,
740 Iacovoni, J.S., Biernacka, A., Skrzypczak, M., Ginalski, K., Rowicka, M., Fraser, P., Legube,
741 G. (2017) Genome-wide mapping of long-range contacts unveils clustering of DNA double-
742 strand breaks at damaged active genes. Nature Structural and Molecular Biology *24*, 353-361.

743 Baumann, C.G., Smith, S.B., Bloomfield, V.A., and Bustamante, C. (1997). Ionic effects on the
744 elasticity of single DNA molecules. Proceedings of the National Academy of Sciences *94*,
745 6185-6190.

746 Baumann, P., Benson, F.E., and West, S.C. (1996). Human Rad51 Protein Promotes ATP-
747 Dependent Homologous Pairing and Strand Transfer Reactions In Vitro. Cell *87*, 757-766.

748 Benson, F.E., Stasiak, A., and West, S.C. (1994). Purification and characterization of the human
749 Rad51 protein, an analogue of E. coli RecA. The EMBO journal *13*, 5764-5771.

750 Brunet, A., Tardin, C., Salome, L., Rousseau, P., Destainville, N., and Manghi, M. (2015).
751 Dependence of DNA Persistence Length on Ionic Strength of Solutions with Monovalent and
752 Divalent Salts : A Joint Theory − Experiment Study. Macromolecules *48*, 3641-3652.

753 Bugreev, D.V., and Mazin, A.V. (2004). Ca2+ activates human homologous recombination protein
754 Rad51 by modulating its ATPase activity. Proceedings of the National Academy of Sciences
755 *101, 9988-93*.

756 Buisson, R., Dion-Côté, A.-M., Coulombe, Y., Launay, H., Cai, H., Stasiak, A.Z., Stasiak, A., Xia,
757 B., and Masson, J.-Y. (2010). Cooperation of breast cancer proteins PALB2 and piccolo
758 BRCA2 in stimulating homologous recombination. Nature structural & molecular biology *17*,
759 1247-1254.

760 Candelli, A., Holthausen, J.T., Depken, M., Brouwer, I., Franker, M.A.M., Marchetti, M., Heller, I.,
761 Bernard, S., Garcin, E.B., Modesti, M.*, et al.* (2014). Visualization and quantification of nascent
762 RAD51 filament formation at single-monomer resolution. Proceedings of the National
763 Academy of Sciences of the United States of America *111*, 15090-15095.

764 Carreira, A., and Kowalczykowski, S.C. (2011). Two classes of BRC repeats in BRCA2 promote
765 RAD51 nucleoprotein filament function by distinct mechanisms. Proceedings of the National
766 Academy of Sciences *108, 10448-53*.

767 Chen, R., and Wold, M.S. (2014). Replication protein A: Single-stranded DNA's first responder.
768 BioEssays *36*, 1156-1161.

769 Chi, Q., Wang, G., and Jiang, J. (2013). The persistence length and length per base of single-
770 stranded DNA obtained from fluorescence correlation spectroscopy measurements using
771 mean field theory. Physica A *392*, 1072-1079.

772 Cho, N.W., Dilley, R.L., Lampson, M.A., Greenberg, R.A. (2014) Interchromosomal homology
773 searches drive directional ALT telomere movement and synapsis. Cell *159*,108-121.

774 Esashi, F., Galkin, V.E., Yu, X., Egelman, E.H., and West, S.C. (2007). Stabilization of RAD51
775 nucleoprotein filaments by the C-terminal region of BRCA2. Nature Structural and Molecular
776 Biology *14*, 468-474.

777 Fan, J., and Pavletich, N.P. (2012). Structure and conformational change of a replication protein A
778 heterotrimer bound to ssDNA. Genes & Development *26*, 2337-2347.

779 Harris, L.A., Hogg, J.S., Tapia, J.J., Sekar, J.A., Gupta, S., Korsunsky, I., Arora, A., Barua, D.,
780 Sheehan, R.P., and Faeder, J.R. (2016). BioNetGen 2.2: advances in rule-based modeling.
781 Bioinformatics *32*, 3366-3368.

782 Hilario, J., Amitani, I., Baskin, R.J., and Kowalczykowski, S.C. (2009). Direct imaging of human
783 Rad51 nucleoprotein dynamics on individual DNA molecules. Proceedings of the National
784 Academy of Sciences *106*, 361-368.

785 Jensen, R.B., Carreira, A., and Kowalczykowski, S.C. (2010). Purified human BRCA2 stimulates
786 RAD51-mediated recombination. Nature *467*, 678-683.

787 Kang, J., Jung, J., and Keun, S. (2014). Flexibility of single-stranded DNA measured by single-
788 molecule FRET. Biophysical Chemistry *195*, 49-52.

789 Ma, C., Kwon, Y., Sung, P., and Greene, E.C. (2017a). Human RAD52 interactions with replication
790 protein A and the RAD51 presynaptic complex. Journal of Biological Chemistry *292*, 11702-
791 11713.

792 Ma, C.J., Gibb, B., Kwon, Y., Sung, P., and Greene, E.C. (2017b). Protein dynamics of human
793 RPA and RAD51 on ssDNA during assembly and disassembly of the RAD51 filament. Nucleic
794 Acids Research *45*, 749-761.

795 Miné, J., Disseau, L., Takahashi, M., Cappello, G., Dutreix, M., and Viovy, J.L. (2007). Real-time
796 measurements of the nucleation, growth and dissociation of single Rad51-DNA nucleoprotein
797 filaments. Nucleic Acids Research *35*, 7171-7187.

798 Miyazaki, T., Bressan, D.A., Shinohara, M., Haber, J.E., and Shinohara, A. (2004). In vivo
799 assembly and disassembly of Rad51 and Rad52 complexes during double-strand break
800 repair. EMBO Journal *23*, 939-949.

801 Murphy, M.C., Rasnik, I., Cheng, W., Lohman, T.M., and Ha, T. (2004). Probing Single-Stranded
802 DNA Conformational Flexibility Using Fluorescence Spectroscopy. Biophysical Journal *86*,
803 2530-2537.

804 Myszka, D.G. (1999). Improving biosensor analysis. Journal of molecular recognition : JMR *12*,
805 279-284.

806 Reuter, M., Zelensky, A., Smal, I., Meijering, E., Cappellen, W.A.V., Gruiter, H.M.D., Belle, G.J.V.,
807 Royen, M.E.V., Houtsmuller, A.B., Essers, J.*, et al.* (2014). BRCA2 diffuses as oligomeric
808 clusters with RAD51 and changes mobility after DNA damage in live cells. Journal of Cell
809 Biology *207*, 599-613.

810 Shahid, T., Soroka, J., Kong, E.H., Malivert, L., McIlwraith, M.J., Pape, T., West, S.C., and Zhang,
811 X. (2014). Structure and mechanism of action of the BRCA2 breast cancer tumor suppressor.
812 Nature Structural and Molecular Biology *21*, 962-968.

813 Shim, K.-s., Schmutte, C., Yoder, K., and Fishel, R. (2006). Defining the salt effect on human
814 RAD51 activities. DNA Repair *5*, 718-730.

815 Short, J.M., Liu, Y., Chen, S., Soni, N., Madhusudhan, M.S., Shivji, M.K.K., and Venkitaraman,
816 A.R. (2016). High-resolution structure of the presynaptic RAD51 filament on single-stranded
817 DNA by electron cryo-microscopy. Nucleic Acids Research *44*, 9017-9030.

818 Sim, A.Y.L., Lipfert, J., Herschlag, D., and Doniach, S. (2012). Salt dependence of the radius of
819 gyration and flexibility of single-stranded DNA in solution probed by small-angle x-ray
820 scattering. Physical Review E *86*, 1-5.

821 Subramanyam, S., Ismail, M., Bhattacharya, I., and Spies, M. (2016). Tyrosine phosphorylation
822 stimulates activity of human RAD51 recombinase through altered nucleoprotein filament
823 dynamics. Proceedings of the National Academy of Sciences *113*, E6045-E6054.

824 Taylor, M.R.G., Ma, C.J., Greene, E.C., Krejci, L., Boulton, S.J., Ma, C.J., Carzaniga, R., Takaki,
825 T., and Collinson, L.M. (2016). A Polar and Nucleotide-Dependent Mechanism of Action for
826 RAD51 Paralogs in RAD51 Filament Article A Polar and Nucleotide-Dependent Mechanism of
827 Action for RAD51 Paralogs in RAD51 Filament Remodeling. Molecular Cell *64*, 926-939.

828 Toni, T., Welch, D., Strelkowa, N., Ipsen, A., and Stumpf, M.P. (2009). Approximate Bayesian
829 computation scheme for parameter inference and model selection in dynamical systems. J R
830 Soc Interface *6*, 187-202.

831 Tubbs, A., and Nussenzweig, A. (2017). Endogenous DNA Damage as a Source of Genomic
832 Instability in Cancer. Cell *168*, 644-656.

833 Tubbs, A., Sridharan, S., van Wietmarschen, N., Maman, Y., Callen, E., Stanlie, A., Wu, W., Wu,
834 X., Day, A., Wong, N., Yin, M., Canela, A., Fu, H., Redon, C., Pruitt, S.C., Jaszczyszyn, Y.,
835 Aladjem, M.I., Aplan, P.D., Hyrien, O., Nussenzweig, A. (2018). Dual Roles of Poly(dA:dT)
836 Tracts in Replication Initiation and Fork Collapse. Cell *174*, 1127-1142.

837 Van der Heijden, T., Seidel, R., Modesti, M., Kanaar, R., Wyman, C., and Dekker, C. (2007). Real-
838 time assembly and disassembly of human RAD51 filaments on individual DNA molecules.
839 Nucleic Acids Research *35*, 5646-5657.

840 Vilenchik, M.M., and Knudson, A.G. (2003). Endogenous DNA double-strand breaks : Production ,
841 fidelity of repair , and induction of cancer. Proceedings of the National Academy of Sciences
842 *100*, 12871-12876.

843 Yu, D.S., Sonoda, E., Takeda, S., Huang, C.L.H., Pellegrini, L., Blundell, T.L., and Venkitaraman,
844 A.R. (2003). Dynamic control of Rad51 recombinase by self-association and interaction with
845 BRCA2. Molecular Cell *12*, 1029-1041.

846 Zhao, W., Vaithiyalingam, S., Filippo, J.S., Chazin, W.J., Wiese, C., Zhao, W., Vaithiyalingam, S.,
847 Filippo, J.S., Maranon, D.G., and Jimenez-sainz, J. (2015). Promotion of BRCA2-Dependent
848 Homologous Recombination by DSS1 via RPA Targeting and DNA Mimicry Article Promotion
849 of BRCA2-Dependent Homologous Recombination by DSS1 via RPA Targeting and DNA
850 Mimicry. Molecular Cell *59*, 176-187.

851 Zhou, Y., Caron, P., Toulouse, F., and Paull, T.T. (2014). Quantitation of DNA double-strand break
852 resection intermediates in human cells. Nucleic Acids Research *42*.

853 Zou, Y.U.E., Liu, Y., Wu, X., and Shell, S.M. (2006). Functions of Human Replication Protein A (
854 RPA): From DNA Replication to DNA Damage and Stress Responses. Journal of Cellular
855 Physiology *273*, 267-273.

856

857 **Table 1. Persistence length of 50-mer DNA oligos**

Oligo Name	Kuhn length (nm)	Persistence length (nm)	Persistence length error (95% CI) (nm)
ssDNA dT-50	2.6702	1.3351	0.200185
ssDNA dN-50	4.5177	2.25885	0.048095
ssDNA dA-50	9.3488	4.6744	0.13126
dsDNA dN-50p	14.674	7.337	0.07379

858

Figure 1

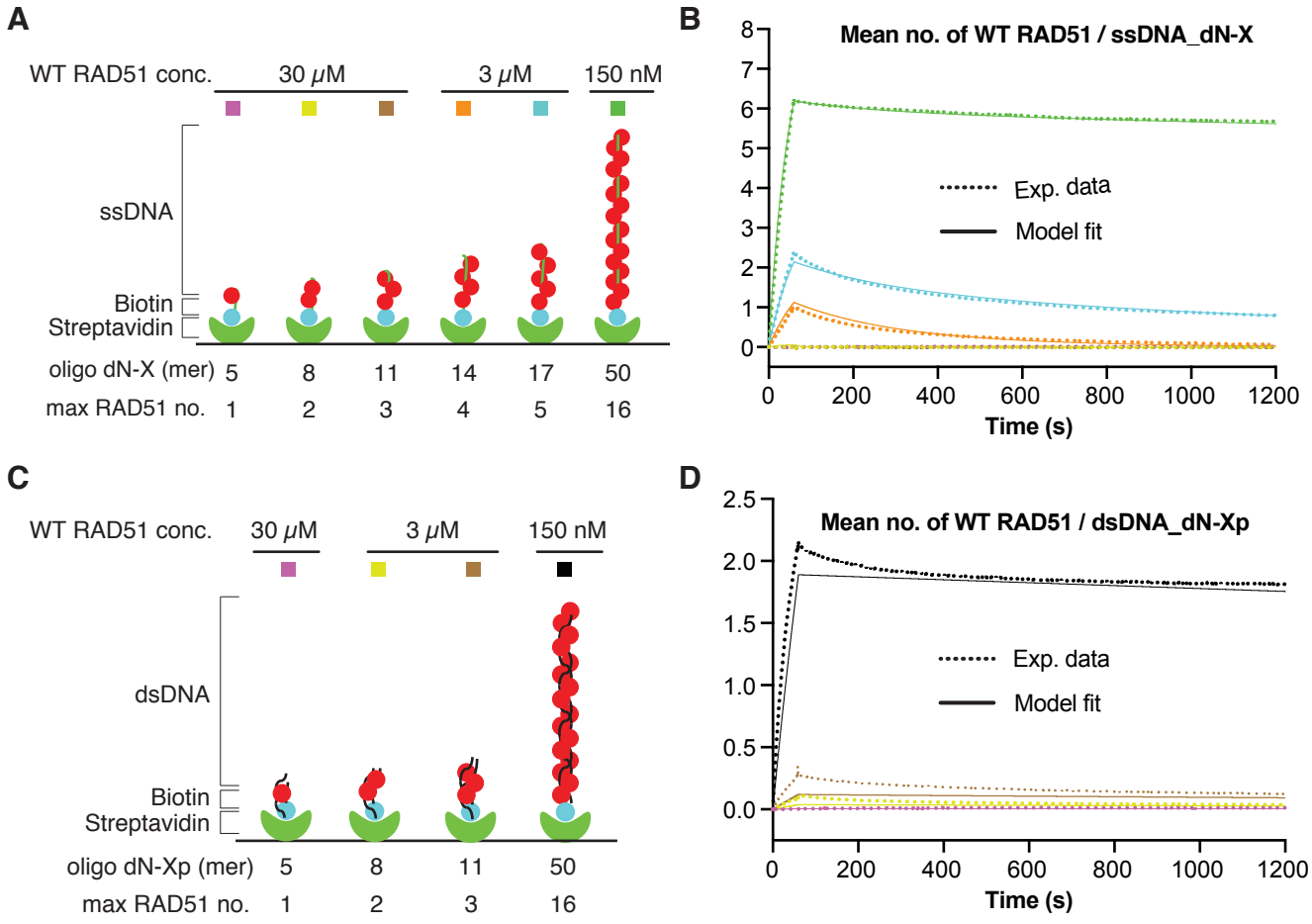
A
WT RAD51 conc.
30 μM
3 μM
150 nM
ssDNA
Biotin
Streptavidin
oligo dN-X (mer) 5 8 11 14 17 50
max RAD51 no. 1 2 3 4 5 16
B
Mean no. of WT RAD51 / ssDNA_dN-X
Exp. data
Model fit
Time (s)
C
WT RAD51 conc.
30 μM
3 μM
150 nM
dsDNA
Biotin
Streptavidin
oligo dN-Xp (mer) 5 8 11 50
max RAD51 no. 1 2 3 16
D
Mean no. of WT RAD51 / dsDNA_dN-Xp
Exp. data
Model fit
Time (s)

Figure 2

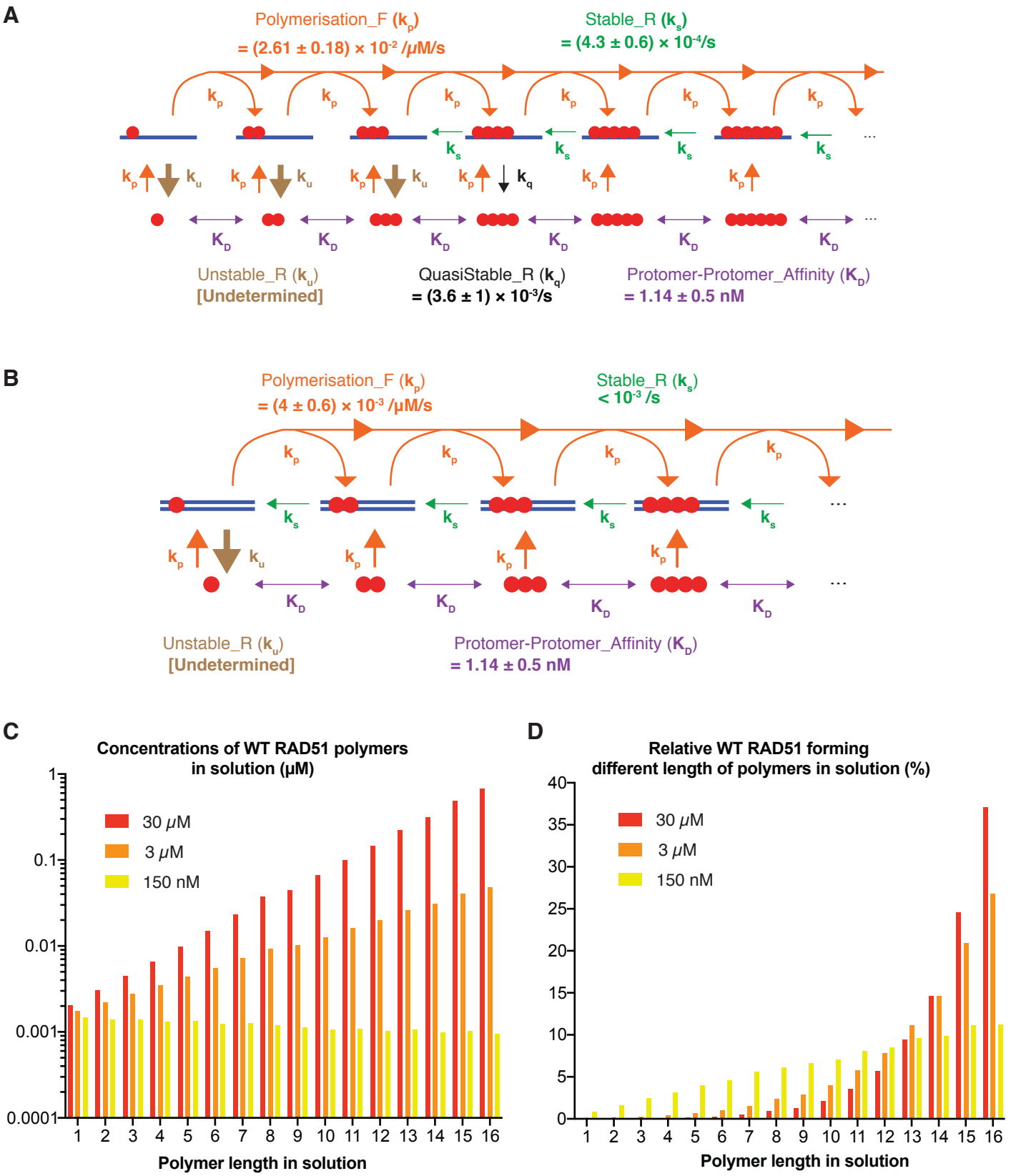
A
Polymerisation_F (kp)
= (2.61 ± 0.18) × 10-2 /μM/s
Stable_R (ks)
= (4.3 ± 0.6) × 10-4/s
Unstable_R (ku)
[Undetermined]
QuasiStable_R (kq)
= (3.6 ± 1) × 10-3/s
Protomer-Protomer_Affinity (KD)
= 1.14 ± 0.5 nM
B
Polymerisation_F (kp)
= (4 ± 0.6) × 10-3 /μM/s
Stable_R (ks)
< 10-3 /s
Unstable_R (ku)
[Undetermined]
Protomer-Protomer_Affinity (KD)
= 1.14 ± 0.5 nM
C
Concentrations of WT RAD51 polymers in solution (μM)
30 μM
3 μM
150 nM
Polymer length in solution
D
Relative WT RAD51 forming different length of polymers in solution (%)
30 μM
3 μM
150 nM
Polymer length in solution

Figure 3

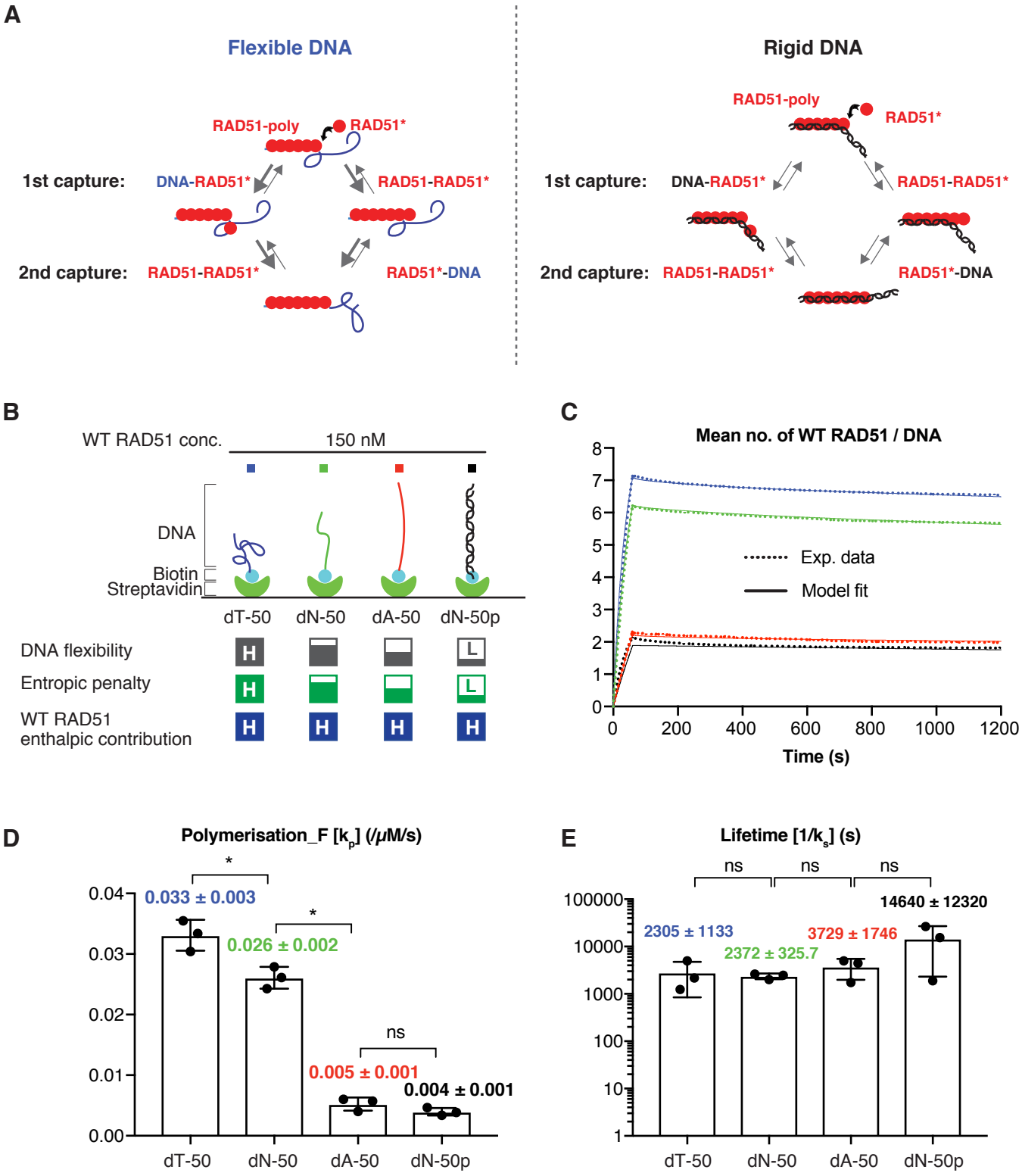
A
Flexible DNA
RAD51-poly
RAD51*
1st capture:
DNA-RAD51*
RAD51-RAD51*
2nd capture:
RAD51-RAD51*
RAD51*-DNA
Rigid DNA
RAD51-poly
RAD51*
1st capture:
DNA-RAD51*
RAD51-RAD51*
2nd capture:
RAD51-RAD51*
RAD51*-DNA
B
WT RAD51 conc.
150 nM
DNA
Biotin
Streptavidin
dT-50
dN-50
dA-50
dN-50p
DNA flexibility
Entropic penalty
WT RAD51
enthalpic contribution
H
L
C
Mean no. of WT RAD51 / DNA
Exp. data
Model fit
Time (s)
D
Polymerisation_F [k_p] (/μM/s)
0.033 ± 0.003
0.026 ± 0.002
0.005 ± 0.001
0.004 ± 0.001
ns
dT-50
dN-50
dA-50
dN-50p
E
Lifetime [1/k_s] (s)
ns
2305 ± 1133
2372 ± 325.7
3729 ± 1746
14640 ± 12320
dT-50
dN-50
dA-50
dN-50p

Figure 4

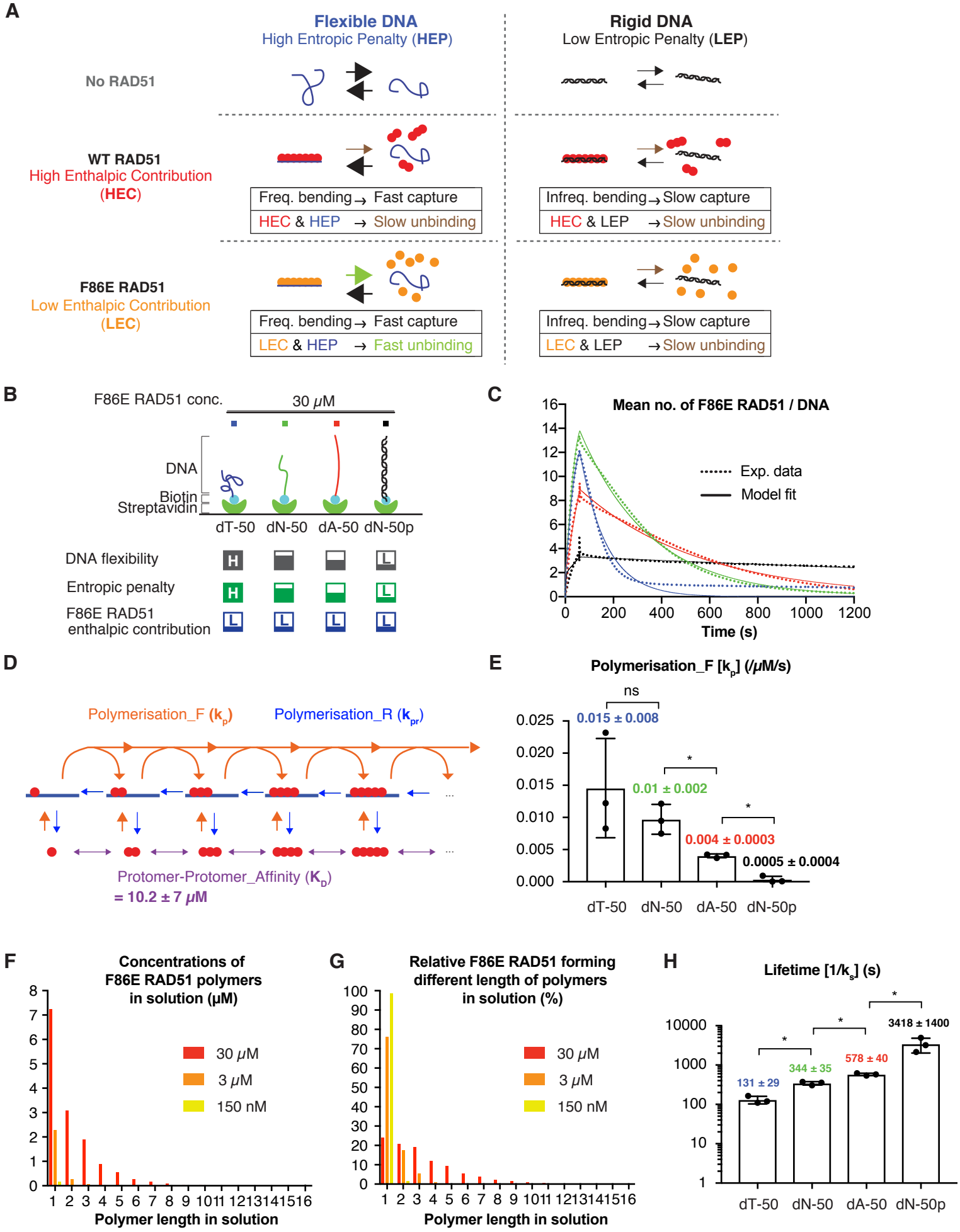
A
Flexible DNA
High Entropic Penalty (HEP)
Rigid DNA
Low Entropic Penalty (LEP)
No RAD51
WT RAD51
High Enthalpic Contribution
(HEC)
Freq. bending → Fast capture
HEC & HEP → Slow unbinding
Infreq. bending → Slow capture
HEC & LEP → Slow unbinding
F86E RAD51
Low Enthalpic Contribution
(LEC)
Freq. bending → Fast capture
LEC & HEP → Fast unbinding
Infreq. bending → Slow capture
LEC & LEP → Slow unbinding
B
F86E RAD51 conc.
30 μM
DNA
Biotin
Streptavidin
dT-50
dN-50
dA-50
dN-50p
DNA flexibility
Entropic penalty
F86E RAD51
enthalpic contribution
H
L
C
Mean no. of F86E RAD51 / DNA
Exp. data
Model fit
Time (s)
D
Polymerisation_F (kp)
Polymerisation_R (kpr)
Protomer-Protomer_Affinity (KD)
= 10.2 ± 7 μM
E
Polymerisation_F [kp] (/μM/s)
ns
0.015 ± 0.008
0.01 ± 0.002
0.004 ± 0.0003
0.0005 ± 0.0004
dT-50
dN-50
dA-50
dN-50p
F
Concentrations of
F86E RAD51 polymers
in solution (μM)
30 μM
3 μM
150 nM
Polymer length in solution
G
Relative F86E RAD51 forming
different length of polymers
in solution (%)
30 μM
3 μM
150 nM
Polymer length in solution
H
Lifetime [1/ks] (s)
131 ± 29
344 ± 35
578 ± 40
3418 ± 1400
dT-50
dN-50
dA-50
dN-50p

Figure S1

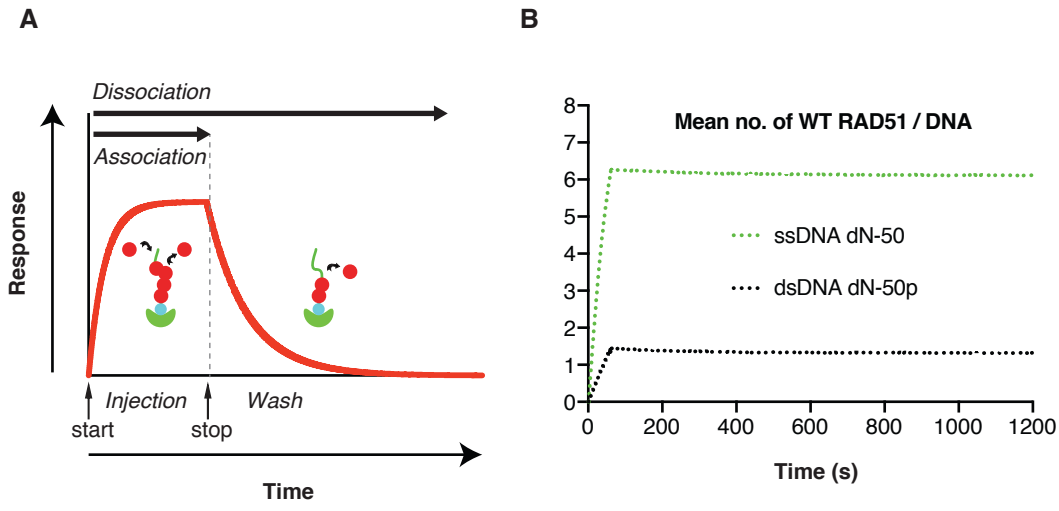
A
Dissociation
Association
Response
Injection
Wash
start
stop
Time
B
Mean no. of WT RAD51 / DNA
ssDNA dN-50
dsDNA dN-50p
0
1
2
3
4
5
6
7
8
0
200
400
600
800
1000
1200
Time (s)

Figure S2

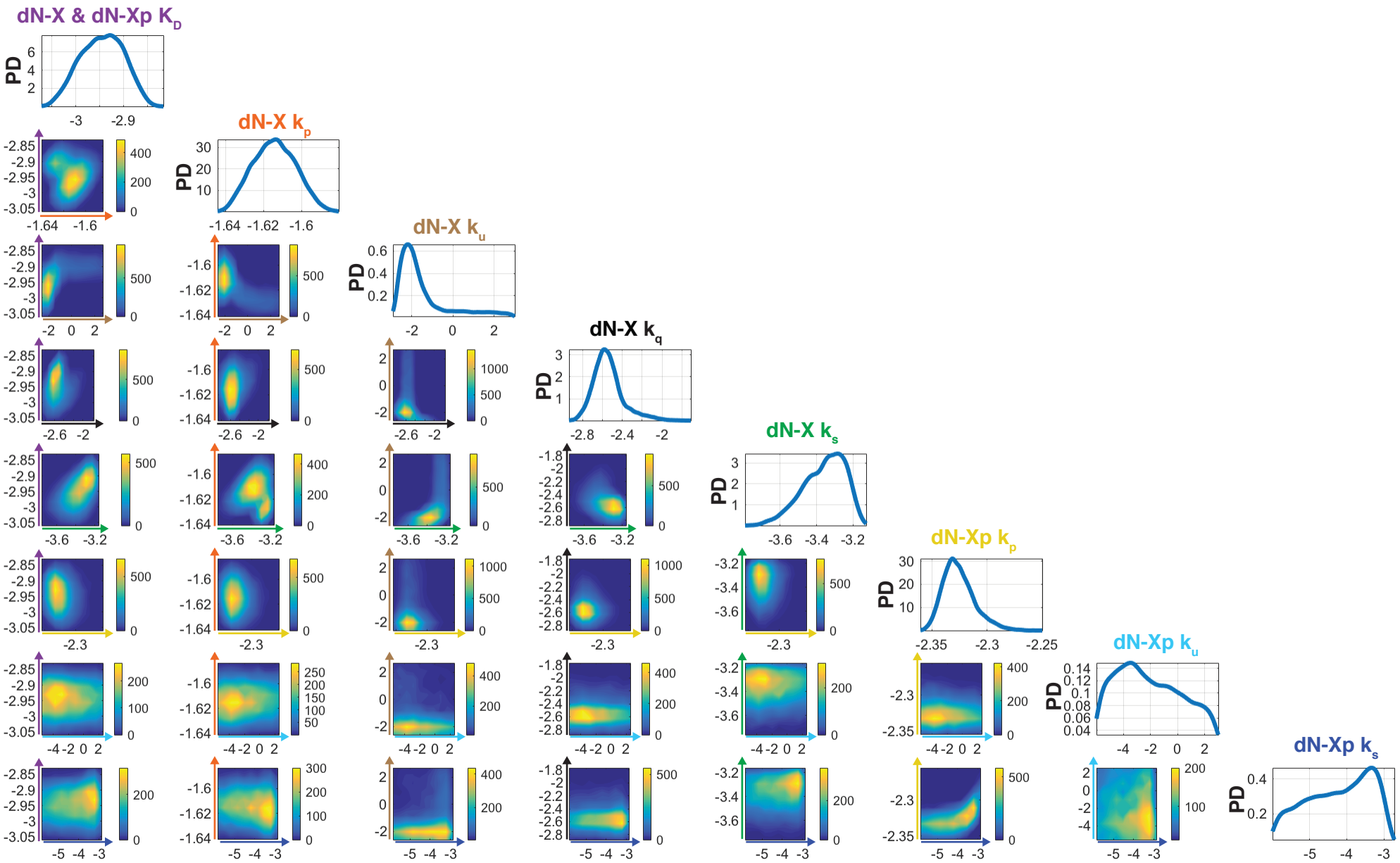

Figure S3

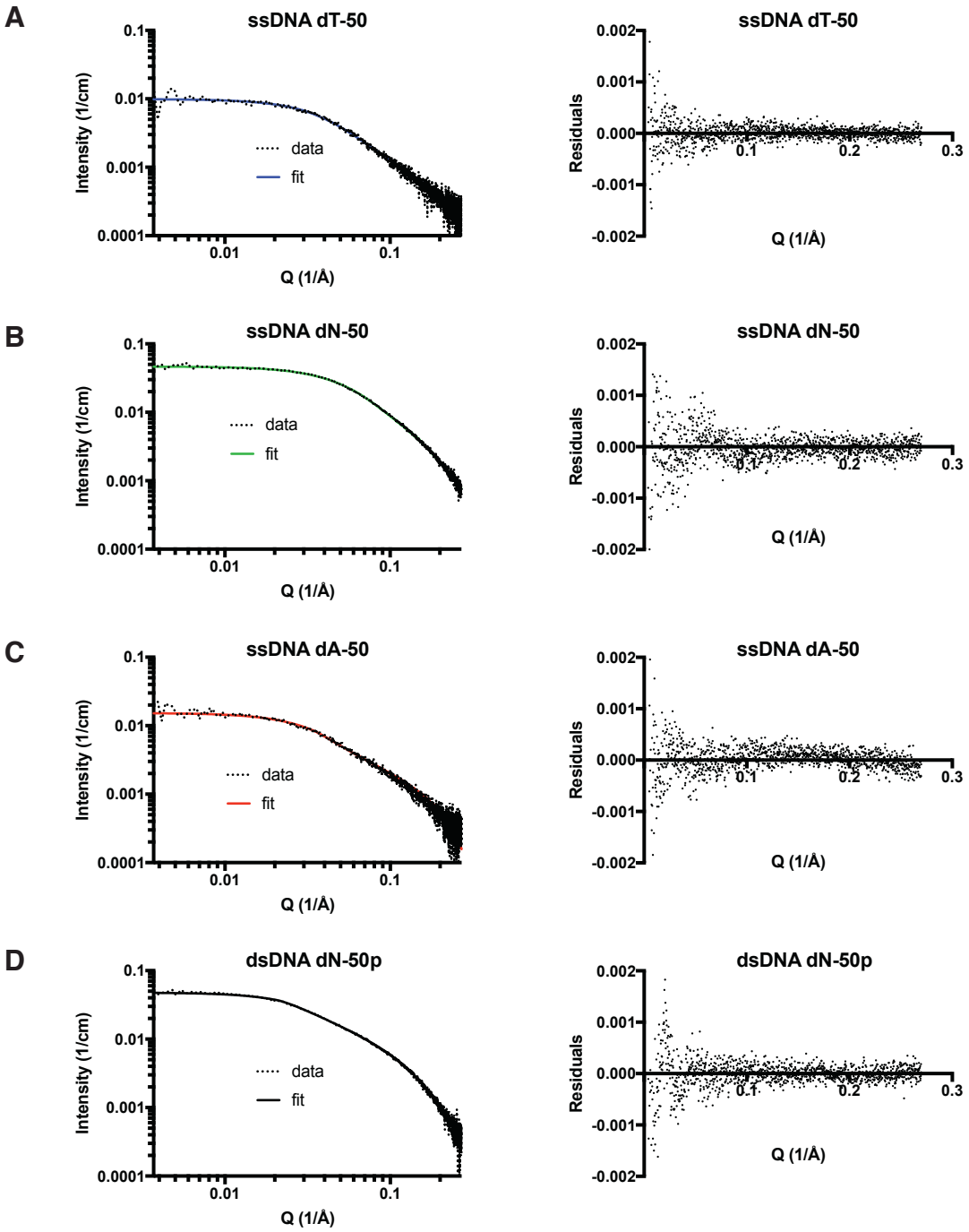
A
ssDNA dT-50
Intensity (1/cm)
0.1
0.01
0.001
0.0001
data
fit
0.01
0.1
Q (1/Å)
ssDNA dT-50
Residuals
0.002
0.001
0.000
-0.001
-0.002
0.1
0.2
0.3
Q (1/Å)
B
ssDNA dN-50
Intensity (1/cm)
data
fit
Q (1/Å)
ssDNA dN-50
Residuals
Q (1/Å)
C
ssDNA dA-50
Intensity (1/cm)
data
fit
Q (1/Å)
ssDNA dA-50
Residuals
Q (1/Å)
D
dsDNA dN-50p
Intensity (1/cm)
data
fit
Q (1/Å)
dsDNA dN-50p
Residuals
Q (1/Å)

Figure S4

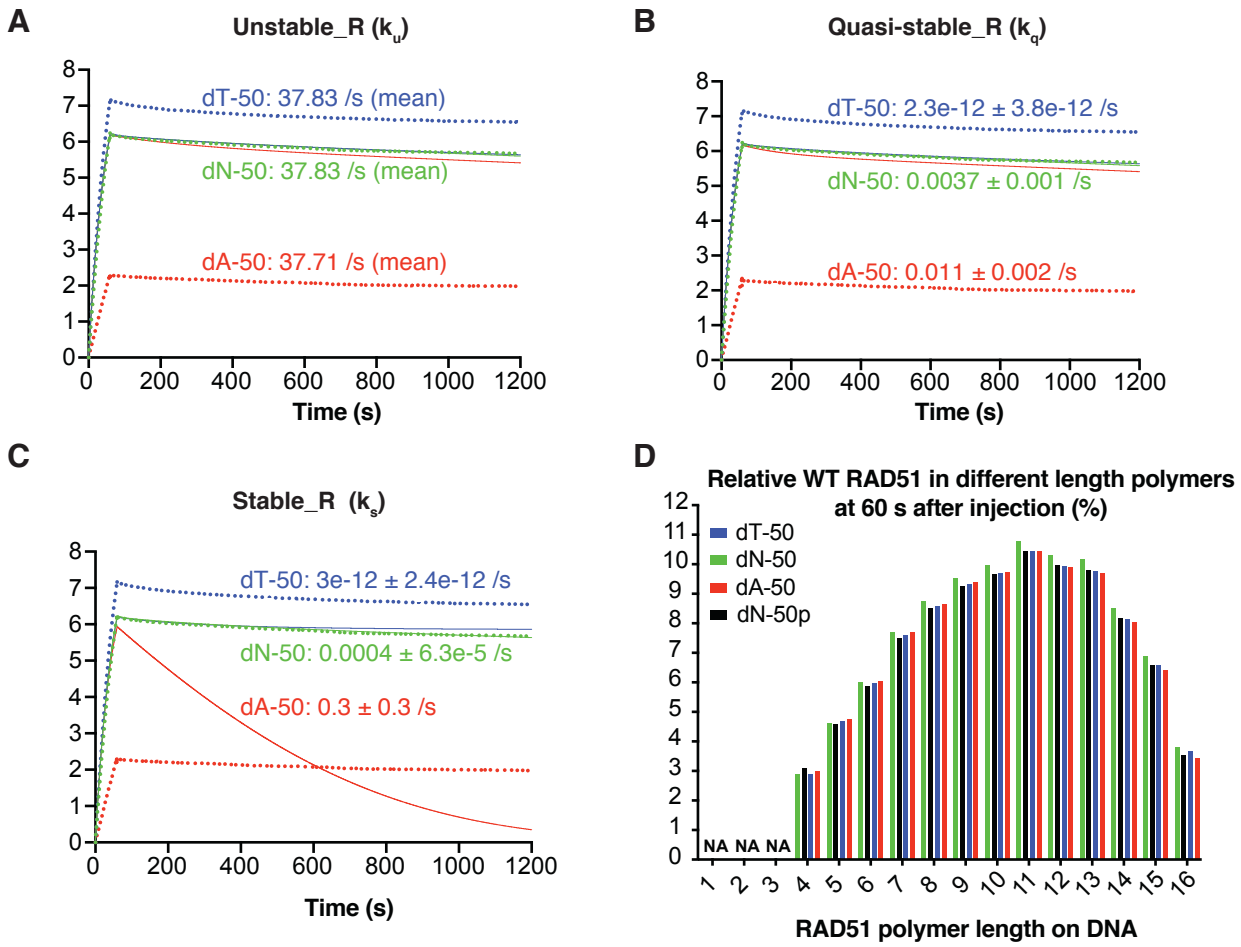
A
Unstable_R (k_u)
dT-50: 37.83 /s (mean)
dN-50: 37.83 /s (mean)
dA-50: 37.71 /s (mean)
Time (s)
B
Quasi-stable_R (k_q)
dT-50: 2.3e-12 ± 3.8e-12 /s
dN-50: 0.0037 ± 0.001 /s
dA-50: 0.011 ± 0.002 /s
Time (s)
C
Stable_R (k_s)
dT-50: 3e-12 ± 2.4e-12 /s
dN-50: 0.0004 ± 6.3e-5 /s
dA-50: 0.3 ± 0.3 /s
Time (s)
D
Relative WT RAD51 in different length polymers at 60 s after injection (%)
dT-50
dN-50
dA-50
dN-50p
NA NA NA
RAD51 polymer length on DNA

Figure S5

A

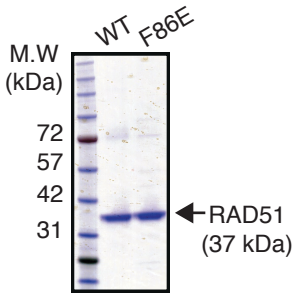

B

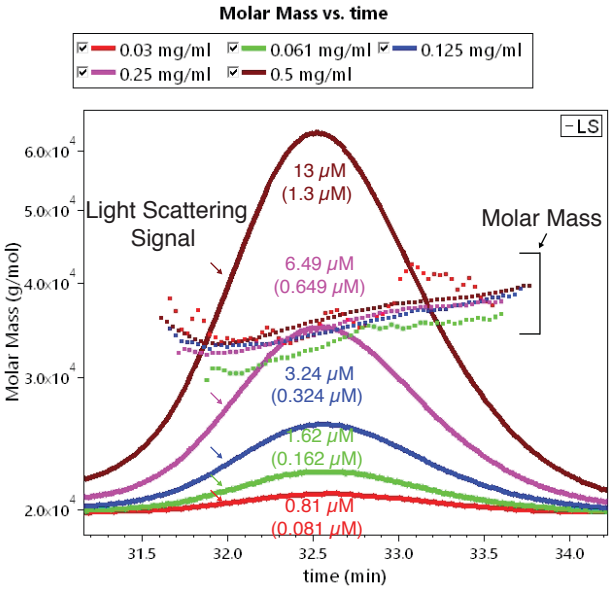

C

[F86E] (mg/ml)	Mw (kDa)	RSE
0.03	36.2	4.6%
0.061	33.3	1.1%
0.125	34.9	0.8%
0.25	34.9	0.2%
0.5	35.9	0.4%
Average	35	

D

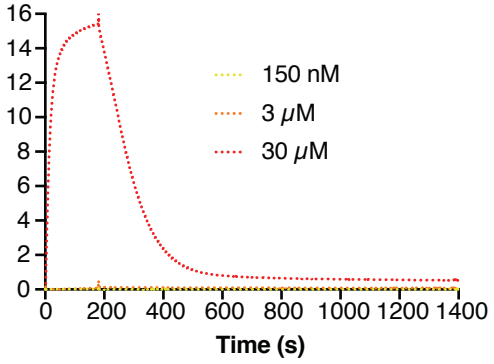

E

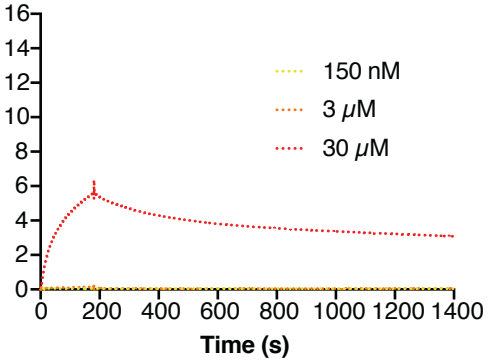

A

Figure S6

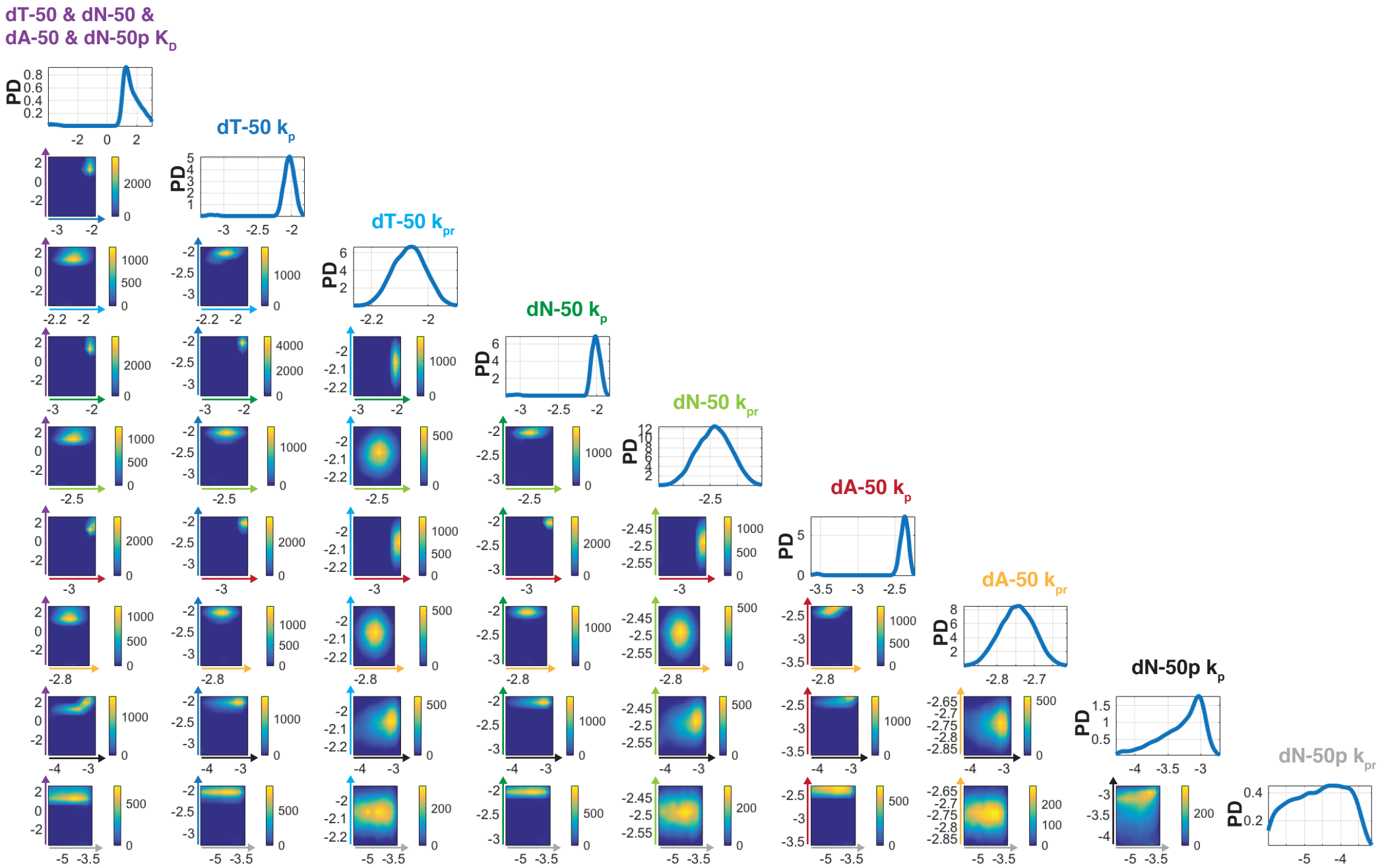
dT-50 & dN-50 &
dA-50 & dN-50p K_D
dT-50 k_p
dT-50 k_{pr}
dN-50 k_p
dN-50 k_{pr}
dA-50 k_p
dA-50 k_{pr}
dN-50p k_p
dN-50p k_{pr}
PD